Petroleum Science 22 (2025) 4538–4554

Contents lists available at ScienceDirect

Petroleum Science

journal homepage: www.keaipublishing.com/en/journals/petroleum-science

Original Paper

Numerical investigations on T_1-T_2*-based petrophysical evaluation in shale oil reservoir with complex minerals

Ji-Long Liu [a,b], Ran-Hong Xie [a,b,*], Jiang-Feng Guo [a,b], Chen-Yu Xu [a,b], Guo-Wen Jin [a,b], Xiang-Yu Wang [a,b], Bo-Chuan Jin [a,b], Xiao-Long Ju [a,b]

[a] State Key Laboratory of Petroleum Resources and Engineering, China University of Petroleum (Beijing), Beijing, 102249, China
[b] Key Laboratory of Earth Prospecting and Information Technology, China University of Petroleum (Beijing), Beijing, 102249, China

ARTICLE INFO

Article history:
Received 19 April 2025
Received in revised form
8 June 2025
Accepted 25 July 2025
Available online 31 July 2025

Edited by Meng-Jiao Zhou

Keywords:
Shale oil
Complex minerals
T_1-T_2*
Petrophysical parameters
Frequency conversion

ABSTRACT

It is of great significance to evaluate the petrophysical properties in shale oil reservoir, which can contribute to geological storage CO_2. Two-dimensional nuclear magnetic resonance (2D NMR) technology has been applied to petrophysical characterization in shale oil reservoir. However, limitations of traditional 2D NMR (T_1-T_2 or T_2-D) in detecting short-lived organic matter and the complexity of mineral compositions, pose NMR-based petrophysical challenges. The organic pores were assumed saturated oil and the inorganic pores were assumed saturated water, and the numerical algorithm and theory of T_1-T_2* in shale oil reservoir were proposed, whose accuracy was validated through T_2, T_1-T_2 and T_2* experiments. The effects of mineral types and contents on the T_1-T_2* responses were firstly simulated by the random walk algorithm, revealing the NMR response mechanisms in shale oil reservoir with complex mineral compositions at different magnetic field frequency (f). The results indicate that when the pyrite content is 5.43%, dwell time is 4 μs, the f is 200 MHz, and echo spacing is 0.4 ms, the T_1-T_2*-based porosity is 2.39 times that of T_1-T_2-based porosity. The T^*_{2LM} is 0.015 ms, which is 0.015 times that of T_{2LM}. The T_{1LM} is 8.84 ms, which is 0.63 times that of T_{1LM}. The T_1-T_2*-based petrophysical conversion models were firstly created, and the foundation of petrophysical conversion was laid at different f.

1. Introduction

Energy affects human development and societal progress. In recent years, clean energy has been continuously developing, but its supply capacity is limited, while ongoing extraction of fossil fuels has led to energy shortages (Cui et al., 2022). Shale reserves are vast, and their effective development can help alleviate energy shortages (Zhou et al., 2023; Saif et al., 2019). Shale oil is extracted from shale through techniques such as pyrolysis and thermal dissolution (Kang et al., 2020; Zou et al., 2010; Li et al., 2022; Liu et al., 2022a; Liu et al., 2022b; Zhang et al., 2019; Ozotta et al., 2022). The situ thermal decomposition technology, economically viable and pollution-free, is considered an effective method for extracting shale oil (Wang et al., 2023; Zhang et al., 2023; Lei et al., 2021). However, since the industrial revolution, people have faced the problem of continuous CO_2 emissions leading to a gradual increase in global temperatures (Leung et al., 2014; Bai et al., 2015; Ershadnia et al., 2022). It is of great significance to achieve geological storage CO_2 in shale reservoirs while obtaining economic benefits from shale oil. Therefore, understanding the petrophysical properties of shale oil reservoir is essential.

NMR logging, a non-destructive, non-invasive technique, has been utilized to the petrophysical characterization (Liu et al., 2024a, 2024b; Xu et al., 2023; Jiang et al., 2023). Traditional 2D NMR logging (T_2-D and T_1-T_2) provides various relaxation time information to accurately characterize the petrophysical properties of conventional reservoirs. However, the measurement effectiveness is poor for shale reservoirs rich in organic matter with low diffusion rates. T_1-T_2* and T_1*-T_2* can compensate for this deficiency. Zamiri et al. (2021) utilized a 100 MHz NMR instrument to measure T_1-T_2 and T_1-T_2* relaxation spectra for quantitatively monitoring variable fluid contents through evaporation and water adsorption/desorption experiments (Zamiri et al., 2021). Guo et al. (2021) utilized T_1-T_2* relaxation spectra to investigate relaxation

* Corresponding author.
E-mail address: xieranhong@cup.edu.cn (R.-H. Xie).
Peer review under the responsibility of China University of Petroleum (Beijing).

https://doi.org/10.1016/j.petsci.2025.07.020

information of solid-state materials (Guo et al., 2021). Guo et al. developed novel technique using T_1*-T_2* relaxation correlation (Guo et al., 2022a, 2022b). In the meanwhile, for quantifying the ^{1}H content in organic matter, Zamiri et al. (2022) employed T_1-T_2* spectra integrated with thermogravimetric analysis and multi-stage pyrolysis experiments (Zamiri et al., 2022). Zamiri et al. (2023) utilized high-field and low-field T_1-T_2* and T_1*-T_2* spectra to identify signals from water, oil, and kerogen. They monitored fluid changes during water uptake/release, evaporation, multi-temperature-stage pyrolysis, and water absorption experiments by T_1-T_2* measurements and NMR imaging (Zamiri et al., 2023). These experiments are impractical to quantify the effect of each factor on petrophysical properties. Additionally, limitations in NMR technology restrict the use of T_1-T_2* and T_1*-T_2* relaxation correlations for measuring petrophysical properties in downhole shale reservoirs, posing challenges for characterizing petrophysical properties based on 2D NMR logging.

2D NMR numerical technology, on the basis of NMR relaxation mechanisms, facilitates the petrophysical conversion between 2D NMR experimental measurements and logging. For the shale oil reservoir, there is a lack of T_1-T_2* theories and only a few researchers have studied the T_1-T_2 relaxation theories and T_2*-based numerical methods in porous media. Drain (1962) considered that the uneven magnetic field generated by loosely packed and densely packed spherical samples widens the NMR spectra. They calculated the magnetic field distribution contributed by neighboring spheres and regions near adjacent spheres (Drain et al., 1962). Brown et al. (1993) suggested that magnetic field exhibited an increasing characteristic, conducting the CPMG and spin echo pulse sequences in porous media, has experimentally confirmed that the transverse surface relaxation rate is related to the frequency and rotational correlation time of hydrogen atoms in pore fluids (Brown et al., 1993). Ford et al. (1993) linearly superposed dipole magnetic fields to study the impact of local magnetic field gradients on NMR spin echoes (Ford et al., 1993). Bergman et al. (1995) proposed NMR relaxation theory for heterogeneous magnetic fields in porous media, and calculated the impact of diffusion time on transverse relaxation rates (Bergman et al., 1995). Sen et al. (1999) suggested that the internal magnetic field (IMF) was influenced by the position of hydrogen nuclei within the pores (Sen et al., 1999). Valckenborg et al. (2002) used a random walk (RW) method to simulate the FID pulse sequence of fluid inside a single spherical pore in porous media. In their simulations, the pores were considered isolated, and a constant gradient in the IMF resulted from the unchanged susceptibility differences between the pore fluid and the matrix (SDPM). Their study revealed that the SDPM led to dephasing of ^{1}H nuclei, and this dephasing behavior was related to the IMF (Valckenborg et al., 2002). Audoly et al. (2003) used numerical simulations to study the non-uniform distribution of IMF in a packed sphere model pore. The results indicate that the IMF is related to the pore structure factor of the porous medium, which can be used to characterize the pore structure (Audoly et al., 2003). Chen et al. (2005) used finite element methods to simulate the microscale distribution of IMFs and gradients Berea sandstone with different water saturation states (Chen et al., 2005). The results indicated that they observed spatial distributions of IMFs and gradients within Berea sandstone that exhibit Lorentzian characteristics. They confirmed that the diffusion-decay internal field method can be used to study pore size distributions, and the Lorentzian distributions are related to the intensity of external magnetic fields (EMF), the SDPM, and the pore structure. It confirms the presence of free induction decay (FID) responses in fluid-saturated media. They derived their theoretical equations, demonstrating a linear relationship between the linewidth of T_2* spectra and the SDPM as well as the intensity of magnetic field. Müller et al. (2005) systematically analyzed specific surface area, porosity, and pore size distribution based on NMR experiments, N_2 adsorption experiments, and measurements of synthetic and natural unconsolidated samples. By comparing longitudinal relaxation times (T_1) and T_2* measured by surface NMR instruments and laboratory NMR instruments, they demonstrated that T_1 shows good correspondence across different frequencies. However, due to the influence of dispersed phases caused by magnetic field inhomogeneity, there is a significant difference in T_2* measured between surface NMR instruments and laboratory NMR instruments. It is suggested that correction factors for T_2 and T_2* in the presence of low concentrations of paramagnetic minerals are in the range of 1.5–2 (Müller et al., 2005). Müller-Petke et al. (2011) found that differences in instrument dead time, magnetic field inhomogeneity, and the instrument frequency can lead to surface NMR measurements indicating lower water content compared to NMR logging (Müller-Petke et al., 2011). Grunewald et al. (2011) established a numerical simulation theory based on FID, investigating the influences of pore size and magnetization from different porous media on surface NMR responses. The results indicate that T_2* is highly sensitive to pore size in low magnetization porous media. As the magnetization of the porous media increases, the sensitivity of T_2* to pore size decreases due to the influence of pore-scale behavior in the porous media. Larger pore sizes exhibit higher scatter effects, and it was confirmed through laboratory NMR experiments (Grunewald et al., 2011).

According to published papers, no reports related to T_1-T_2* numerical method relaxation theory have been found for shale oil reservoir. In the meanwhile, no reports T_1-T_2* numerical investigations related to the heterogeneity of organic matter and mineral distributions have been found. No reports on T_1-T_2*-based petrophysical conversions have been found.

Currently, the T_1-T_2*-based numerical algorithm and theory in shale oil are still in the exploratory stage. Despite the challenges, the T_1-T_2*-based relaxation theory specific to shale oil reservoir was firstly proposed in this paper. Different from the previous method, heterogeneity of mineral distribution was considered, and the T_1-T_2* numerical simulation method was firstly proposed in shale oil reservoir. The influences of complex minerals on the T_1-T_2* responses were firstly simulated by the improved RW algorithm, revealing the T_1-T_2* response mechanisms at different magnetic field frequencies (f) in shale oil reservoir with complex minerals. Additionally, the T_1-T_2*-based petrophysical models were firstly established.

2. Theory

2.1. T_1-T_2* relaxation theory

Shale reservoirs consist of inorganic and organic pores. Typically, the former is considered water-wet, while the latter is oil-wet (Yang et al., 2018). The organic pores were assumed saturated oil and the inorganic pores were saturated water. On the basis of the T_2* and T_1-T_2 relaxation theory (Liu et al., 2025; Liu et al., 2024c), the T_1-T_2* relaxation theory of pore fluids is proposed, expressed as:

$$\begin{cases} \dfrac{1}{T^*_{2,\mathrm{L}}} = \dfrac{1}{T_{2\mathrm{ori,L}}} + \dfrac{1}{T_{2\mathrm{Lm}}} + \dfrac{1}{T_{2\mathrm{Li}}} \\ \dfrac{1}{T_{1,\mathrm{L}}} = \dfrac{1}{T_{1\mathrm{RB,L}}} + \dfrac{1}{T_{1\mathrm{TB,L}}} + \dfrac{1}{T_{1\mathrm{S,L}}}, \end{cases} \tag{1}$$

where L is oil (O) or water (W), $1/T^*_{2,\mathrm{L}}$ is the effective spin-spin relaxation rate from fluids. $1/T_{2\mathrm{ori,L}}$ are the relaxation rates of

fluids. $1/T_{2Lm}$ and $1/T_{2Li}$ are the spin-spin relaxation rate at the influence of external and IMFs. $1/T_{1RB,L}$ and $1/T_{1TB,L}$ are the longitudinal bulk relaxation rates correspond to intramolecular and intermolecular dipole-dipole interactions, respectively. In practical T_1-T_2* measurements, the EMF is uniform, so $1/T_{2Lm}$ is 0.

The bulk relaxation time (T_{2B}) for fluids were determine by the L-S model (Lipari et al., 1982; Liu et al., 2024a) and the B-P-P model (Tandon et al., 2017; Bloembergen et al., 1948). Meanwhile, according to the Chen et al.'s research (Chen et al., 2005), the relaxation rate corresponding to the IMF is shown as:

$$\frac{1}{T_{2Li}}=\frac{\gamma\cdot C_1\cdot\Delta\chi\cdot B_0}{2}, \tag{2}$$

In Eq. (1), $1/T_{2ori,L}$ can be expressed as:

$$\frac{1}{T_{2ori,L}}=\frac{1}{T_{2B,L}}+\frac{1}{T_{2S,L}}, \tag{3}$$

Eq. (2) and Eq. (3) were substituted Eq. (1), for simplification, it can be expressed as:

$$\begin{cases}\dfrac{1}{T_{2,L}^*}=\dfrac{1}{T_{2B,L}}+\dfrac{1}{T_{2S,L}}+E'\cdot\gamma\cdot\Delta\chi_1\cdot B_0\\ \dfrac{1}{T_{1,L}}=\dfrac{1}{T_{1RB,L}}+\dfrac{1}{T_{1TB,L}}+\dfrac{1}{T_{1S,L}},\end{cases} \tag{4}$$

where $E' = C_1/2$, which is determined by FID experiments. The pores were assumed the cylindrical structure extending along the pore wall (Liu et al., 2024a), and the transverse and longitudinal relaxavities ($\rho_{2S,W}$, $\rho_{2S,O}$, $\rho_{1S,W}$ and $\rho_{1S,O}$) can be shown as:

$$\begin{cases}\rho_{2S,W}=\dfrac{B}{2}\cdot\left(2J_{2D}(0)+\dfrac{3}{4}J_{2D}(\omega_I,\tau)+\dfrac{13}{4}J_{2D}(\omega_S,\tau)\right)\\ \rho_{2S,O}=\dfrac{C}{2}\cdot\left(J_{1D}(0)+\dfrac{3\sqrt{2}}{8}J_{1D}(\omega_I,\tau)+\dfrac{13\sqrt{2}}{8}J_{1D}(\omega_S,\tau)\right)\\ \rho_{1S,W}=\dfrac{B}{4}\cdot(3J_{2D}(\omega_I,\tau)+7J_{2D}(\omega_S,\tau))\\ \rho_{1S,O}=\dfrac{C}{4}\cdot(3J_{1D}(\omega_I,\tau)+7J_{1D}(\omega_S,\tau)),\end{cases} \tag{5}$$

where C and B are parameters associated with the fluid characteristics and pore structure. J_{1D} and J_{2D} represent the spectral density functions related to one-dimensional motion and two-dimensional translational motion, respectively.

The pore structure and fluid properties in shale reservoirs remain constant. Therefore, when the EMF is constant, the $\rho_{2S,W}^*$, $\rho_{2S,O}^*$, $\rho_{1S,W}^*$ and $\rho_{1S,O}^*$ based on the saturation recovery-free induction decay (SR-FID) pulse sequence remain unchanged and can be expressed as:

$$\begin{cases}\rho_{2S,W}^*=\dfrac{B}{2}\cdot\left(2J_{2D}(0)+\dfrac{3}{4}J_{2D}(\omega_I,\tau)+\dfrac{13}{4}J_{2D}(\omega_S,\tau)\right)\\ \rho_{2S,O}^*=\dfrac{C}{2}\cdot\left(J_{1D}(0)+\dfrac{3\sqrt{2}}{8}J_{1D}(\omega_I,\tau)+\dfrac{13\sqrt{2}}{8}J_{1D}(\omega_S,\tau)\right)\\ \rho_{1S,W}^*=\dfrac{B}{4}\cdot(3J_{2D}(\omega_I,\tau)+7J_{2D}(\omega_S,\tau))\\ \rho_{1S,O}^*=\dfrac{C}{4}\cdot(3J_{1D}(\omega_I,\tau)+7J_{1D}(\omega_S,\tau)),\end{cases} \tag{6}$$

where $\rho_{2S,W}^*$, $\rho_{2S,O}^*$, $\rho_{1S,W}^*$, and $\rho_{1S,O}^*$ have been determined by the NMR experiments at different f (Liu et al., 2024a). The magnetic field heterogeneity between organic matter and shale matrix was considered, and the P model is used to calculate the bulk relaxation time of organic matter (Singer et al., 2020), proposing the T_1-T_2* relaxation theory, which can be expressed as:

$$\begin{cases}\dfrac{1}{T_{2S,L}^*}=\dfrac{1}{T_{2S,L}}+E'\cdot\gamma\cdot\Delta\chi_1\cdot B_0+\dfrac{1}{T_{2B,L}}\\ \dfrac{1}{T_{2B,K}^*}=\dfrac{1}{T_{2B,K}}+E'\cdot\gamma\cdot\Delta\chi_2\cdot B_0\\ \dfrac{1}{T_{1,L}}=\dfrac{1}{T_{1RB,L}}+\dfrac{1}{T_{1TB,L}}+\dfrac{1}{T_{1S,L}}\\ \dfrac{1}{T_{1,K}}=\dfrac{1}{T_{1B,K}},\end{cases} \tag{7}$$

2.2. T_1-T_2* numerical simulation method

Based on the T_1-T_2* relaxation theory, numerical simulations can be conducted using the SR-FID pulse sequence (Fig. 1). This pulse sequence requires a short polarization time. Here, SR is used to encode T_1, while FID is used to encode T_2*.

The T_W can be used to acquire the echo data, which can be shown as:

$$\begin{aligned}Echo(T_W,t)=&\iint K_1(T_W,T_1)f(T_1,T_2{}^*)K_2(t,T_2{}^*)\mathrm{d}T_1\mathrm{d}T_2{}^*\\&+Noise(T_W,t)\end{aligned} \tag{8}$$

where $K_1(T_W,T_1)=\left[1-\exp\left(-\frac{T_W}{T_1}\right)\right]$, and $K_2(t,T_2{}^*)=\exp\left(-\frac{t}{T_2{}^*}\right)$ are the kernel functions related to the T_1 and T_2. $Noise(T_W,t)$ is the random noise.

The RW method has been employed for NMR numerical simulation in shale reservoirs (Liu et al., 2024a, 2024b, 2024c). Based on previously constructed digital cores with complex multiple components in the study area (Liu et al., 2023), it was firstly proposed to use the RW method to simulate SR-FID pulse sequences. During T_1 editing, the hydrogen nuclei in fluids undergo inelastic collisions with pore surfaces, then the hydrogen nuclei is polarized, and it goes through the T_2* measurement. The amplitude can be shown as:

$$\mathrm{AMP}_3=\mathrm{AMP}_2\cdot\left(1-\frac{2}{3}\cdot\frac{\rho_{2S,L}r}{D}\cdot 0.96\right), \tag{9}$$

During the T_2* acquisition phase, effected by the heterogeneous internal magnetic field gradients, the hydrogen nuclei undergo diffusion due to non-elastic collisions between pore surfaces and the pore fluid, which can be represented as:

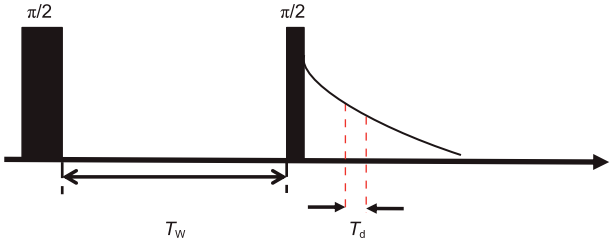

Fig. 1. Schematic diagram of the SR-FID pulse sequence. T_w, waiting time; T_d, dwell time.

$$M_D(t) = M_{D_0}\exp(E'\cdot i\gamma B_0 t)\frac{1}{M}\sum_{m=1}^{M}\cdot\exp(E'\cdot i\gamma z_{n0}t)\cdot\frac{1}{P}\sum_{p=1}^{P}\exp\left(E'\cdot i\gamma G\int_0^t z^p(\tau)\mathrm{d}\tau\right) \tag{10}$$

where $M_{D_0}\exp(E'\cdot i\gamma B_0 t)$ represents the contribution to the phase from EMF. It does not lead to phase accumulation. M_{D_0} represents the initial magnetization of each hydrogen nuclei. P represents the number of hydrogen nuclei. Z_{n0} represents the initial position of the m-th pore voxel. $\int_{p=1}^{P} z^p(\tau)\mathrm{d}\tau$ represents the change in phase of the p-th hydrogen nucleum. P represents the number of hydrogen nucleum.

Therefore, the expression for the phase decay of the FID is obtained as:

$$M_D(t) = \frac{1}{M}\sum_{m=1}^{M}\cdot\exp(E'\cdot i\gamma z_{m0}t)\cdot\frac{1}{P}\sum_{p=1}^{P}\exp\left(E'\cdot i\gamma G\int_0^t z^p(\tau)\mathrm{d}\tau\right) = M'_D(t)\cdot M''_D(t), \tag{11}$$

when the FID was simulated, the diffusion relaxation magnetization of each particle can be computed using its cosine phase, expressed as:

$$\begin{cases} M'_D(t) = \dfrac{1}{M}\displaystyle\sum_{i=1}^{M}\cos(E'\cdot\phi_{0i}(t)) \\ M''_D(t) = \dfrac{1}{P}\displaystyle\sum_{i=1}^{P}\cos(E'\cdot\phi_{1i}(t)), \end{cases} \tag{12}$$

For the i-th proton (^{1}H) at each time step, the phase offset generated by spin can be shown as:

$$\begin{cases} \phi_0(t+\Delta t) = \phi_0(t) + \gamma G_z\cdot\left(\dfrac{z_0(t+\Delta t)+z_0(t)-2z_0(0)}{2}\right)\cdot\mathrm{Resolution}\cdot k\cdot T_d \\ \phi_1(t+\Delta t) = \phi_1(t) + \gamma G_z\cdot\left(\dfrac{z(t+\Delta t)+z(t)-2z(0)}{2}\right)\cdot\Delta t + \gamma G_z\cdot\sqrt{\dfrac{D\cdot\Delta t^3}{6}}\cdot\mathrm{Normal}(), \end{cases} \tag{13}$$

where "Resolution" represents the resolution for multicomponent digital shale core. $z_0(t+\Delta t)$, $z_0(t)$, and $z_0(0)$ are the initial position of ^{1}H in digital shale core at the $t+\Delta t$, t, and initial time. Normal() is the Gaussian function.

After the changed phase is simulated by Eq. (13), the $1/T_{2B,L}$ and $1/T^*_{2B,K}$ were incorporated, the SR-FID simulations completed, as illustrated in Fig. 2.

3. Experimental

3.1. Research plan

The cores come from Chang 7 member of the Ordos Basin. Based on experiments including organic carbon analysis, T_2 experiments at different frequencies, T_1-T_2 experiment, T_2* experiment, and X-ray diffraction quantitative analysis (XRD), geochemical characteristics of the study area were determined through multi-stage thermal decomposition experiments (parallel sample #C-1). The focused ion beam scanning electron microscopy (FIB-SEM) experiments, XRD experiments, and quantitative evaluation of minerals by scanning electron microscopy (QEMSCAN) experiments were used to create the digital shale core representing the shale oil reservoir (Fig. 3(a)). This multi-component digital shale core exhibits both the characteristics of micro-scale pore fluid distribution and the mineral distribution constrained at macro-scale by XRD. Gas chromatography experiments, different frequency NMR T_2 experiments, T_2* experiments, and inversion recovery-Carr-Purcell-Meiboom-Gill (IR-CPMG) experiments (Fig. 3(c)) were conducted to determine the ρ_2, ρ_1, and T_{2B} of pore fluids (Fig. 3(b)).

3.2. Multi-temperature pyrolysis experiments

Based on TOC experiment, #C-1 sample was crushed into fragments smaller than 100 mesh and subjected to multi-temperature pyrolysis experiments using a rock pyrolysis instrument. The heating rate during pyrolysis was 25 °C/min. $S_{1\text{-}1}$ was analyzed under isothermal conditions at 200 °C for 3 min, $S_{1\text{-}2}$ at 350 °C for 3 min, $S_{2\text{-}1}$ at 450 °C for 3 min, and $S_{2\text{-}2}$ at 600 °C for 3 min. Consequently, geochemical parameters for parallel sample #C-1 were obtained as shown in Table 1.

The results indicate that the sample exhibits a low T_{max}, suggesting low organic matter maturity. The sum of $S_{1\text{-}1}$ and $S_{1\text{-}2}$ proportions exceeds 50%, indicating a high movable oil content, while the proportion of $S_{2\text{-}1}$ is relatively high, indicating a high adsorbed oil content, which correlates with the low thermal evolution in this region. Additionally, low TOC suggests low organic richness in this area. The results are consistent with the geochemical patterns of the area.

3.3. Parameter calibration

In previous studies, based on T_2 experiments at different frequencies, extraction, and gas chromatography, the transverse surface relaxavities of fluids, as well as the bulk relaxation times of each fluid component, were determined (Liu et al., 2024a). Due to the consistent fluid properties, the ρ_{1S} of water and oil remain unchanged. As described in Section 2.1, the transverse surface relaxavities and T_{2B} of water and oil at different f are presented in Table 2. They can be utilized for SR-FID numerical simulations.

3.4. Result validation

Based on the T_1-T_2 experimental results, peak values of T_1 were determined as 124 ms, 240.4 ms, and 21.5 ms for organic matter, oil, and water, respectively. Their simulation results were 155 ms, 178.6 ms, and 31.3 ms, respectively. The experimental and numerical results of T_1 value for each component were shown in Fig. 4(a). From Fig. 4(a), they are distributed along the 45° line. Based on the T_2* experimental results, the peak values of T_2* were determined as 0.033 ms, 0.222 ms, and 0.222 ms for organic matter, oil, and water. Their simulation results were 0.038 ms, 0.169 ms, and 0.068 ms. The results indicate that the experimental T_2* value for water is bigger than the simulation, while the peak value T_2 for oil is similar to the simulation (Fig. 4(b)). This is attributed to oil being present in organic pores and water being present in inorganic pores, and significant SDPM causing T_2 of water to move more towards shorter relaxation times. The T_2* values between numerical and experimental results show similar value, validating the accuracies of T_1-T_2* numerical study and relaxation theory.

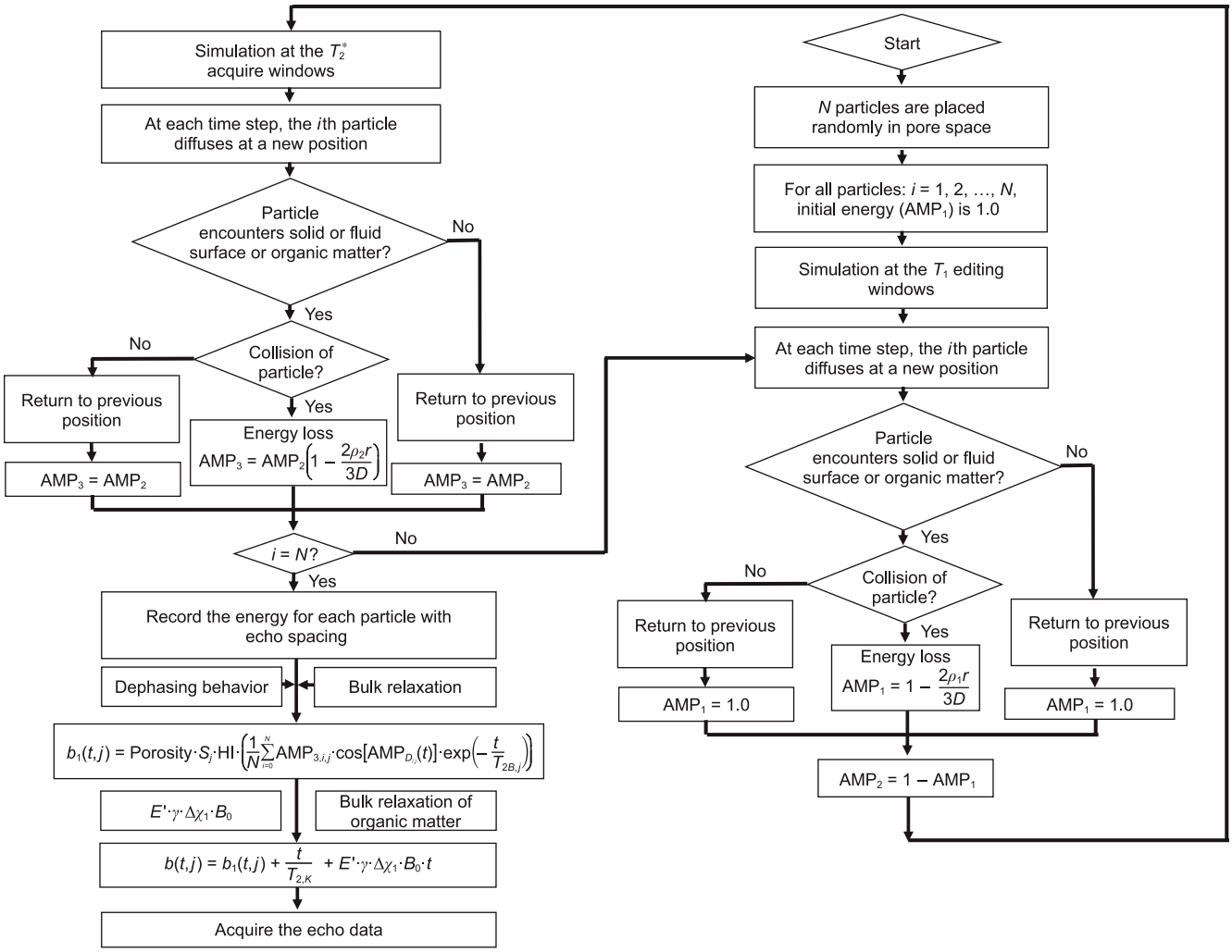

Fig. 2. Flow diagram for SR-FID pulse sequence simulation.

4. Numerical simulation

4.1. Pyrite contents

Based on the T_1-T_2* relaxation theory in shale oil reservoir, the improved RW method proposed in Section 2.2 was used to simulate the T_1-T_2* responses at different pyrite contents. The T_1-T_2* spectra for different f, dwell times (T_d), and pyrite contents were acquired by using the B-R-D method (Butler et al., 1981) for inversion, as shown in Fig. 5. Each plot, includes subplots for oil and water, used to describe the T_1-T_2* responses of pore fluids. The blue, cyan, purple, green, and black lines are T_1-T_2* spectra for pyrite contents of 5.43%, 4.45%, 3.47%, 2.49%, and 1.51%, respectively. The results indicate that, both the T_{1B} and $T^*_{2B,K}$ values of organic matter increase with the increased f, and the mobility for T_{1B} of organic matter is higher than $T^*_{2B,K}$. An increased pyrite content is considered to not alter the SDPM. The T_2* and T_1 of organic matter do not move with an increased pyrite content. The T_1 of pore fluids increase with an increased f, due to the frequency-dependent of ρ_{1S} for the pore fluids. The T_2* of pore fluids decrease with the increased pyrite content and f. Their increases can lead to the enhanced $M_D(t)$, resulting in the left shift of the peak for T_2* distribution, decreased signal intensity and sparse contour lines of fluid signals.

4.2. Clay contents

Based on the T_1-T_2* relaxation theory in shale oil reservoir, the improved RW method proposed in Section 2.2 was used to simulate the T_1-T_2* responses at different clay contents. The T_1-T_2* spectra for different f, T_d, and clay contents were obtained by using the B-R-D method (Butler et al., 1981) for inversion, as shown in Fig. 6. Each plot, includes subplots for oil and water, used to describe the T_1-T_2* responses of pore fluids. The blue, cyan, purple, green, and black lines are T_1-T_2* spectra for clay contents of 4.0%, 8.0%, 12.0%, 16.0%, and 20.0%, respectively. The results indicate that, both the T_{1B} and $T^*_{2B,K}$ values of organic matter increase with the increased f, and the mobility for T_{1B} of organic matter is higher than $T^*_{2B,K}$. An increased clay content is considered to not alter the SDPM. The T_2* and T_1 of organic matter do not move with an increased clay content. The T_1 of pore fluids increase with an increased f, due to the frequency-dependent of ρ_{1S} for the pore fluids. The T_2* of pore fluids

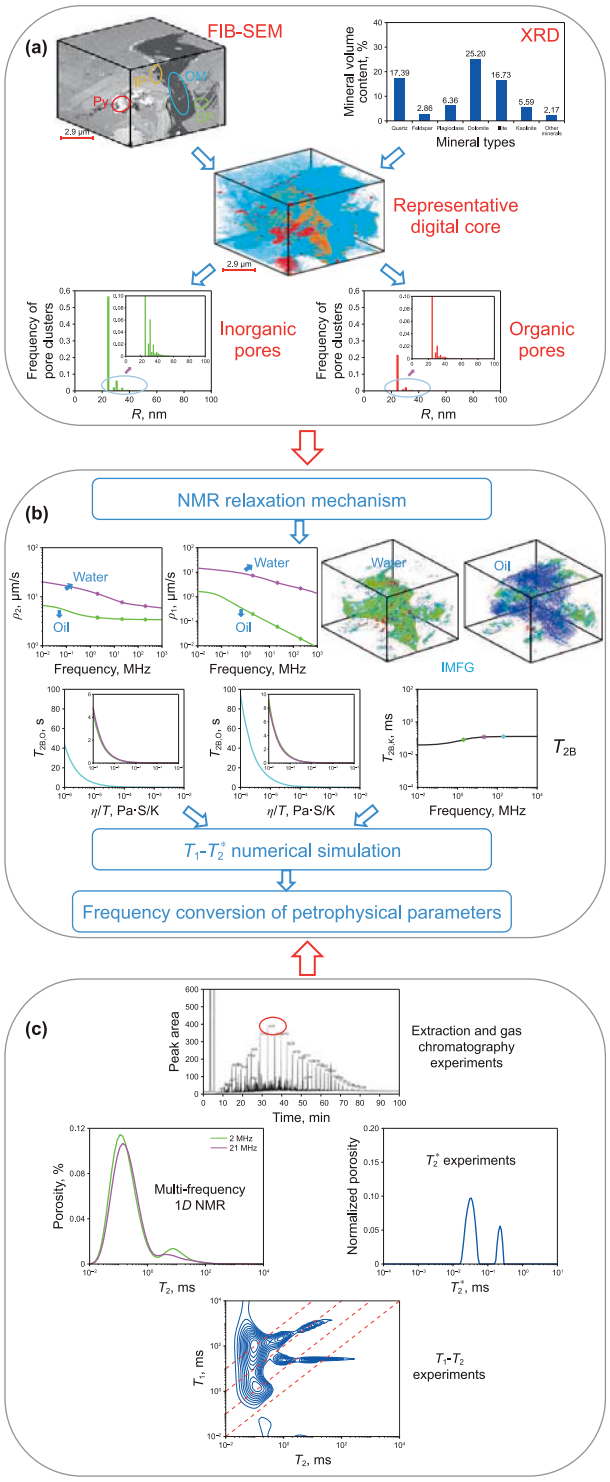

Fig. 3. Experimental process and parameters estimation.

Table 1
Data table for multi-temperature pyrolysis and organic carbon experiment.

Sample	TOC, %	T_{max}, °C	$S_{1\text{-}1}$, mg/g	$S_{1\text{-}2}$, mg/g	$S_{2\text{-}1}$, mg/g	$S_{2\text{-}2}$, mg/g
# C-1	1.16	440	2.44	3.52	2.24	1.33

Table 2
Data from T_1-T_2* parameter.

f, MHz	ρ_{2S}, μm/s		ρ_{1S}, μm/s		T_{2B}, s			FID parameters	
	W	O	W	O	W	O	OM	E'	$\Delta\chi$
21.36	7.65	3.50	3.7	0.06	2.6	1.1	0.12×10^{-3}	0.01	9×10^{-5}SI
100	6.30	3.45	3.32	0.027	2.6	1.1	0.13×10^{-3}	0.01	9×10^{-5} SI
200	6.13	3.40	2.9	0.02	2.6	1.1	0.13×10^{-3}	0.01	9×10^{-5} SI

Note: W represents water, O represents oil, and OM represents organic matter.

decrease with the increased clay contents and f. The increased clay content, f, and T_d can result in the increase in $M_D(t)$, resulting in the left shift of the peak for T_2* distribution, decreased signal intensity and sparse contour lines of fluid signals.

4.3. Clay types

Based on the T_1-T_2* relaxation theory in shale oil reservoir, the improved RW method proposed in Section 2.2 was used to simulate the T_1-T_2* responses at different clay types. The T_1-T_2* spectra for different f, T_d, and clay types were obtained by using the B-R-D method (Butler et al., 1981) for inversion, as shown in Fig. 7. Each plot, includes subplots for oil and water, used to describe the T_1-T_2* response of pore fluids. The black, and green lines represent the T_1-T_2* spectra for clay types of montmorillonite and chlorite, respectively. The results indicate that, both the T_{1B} and T_{2B}^* values of organic matter increase with the increased f, and the mobility for T_{1B} of organic matter is higher than T_{2B}^*. An increased magnetic susceptibility is considered to not alter the SDPM. The T_2* and T_1 of organic matter do not move with the changed clay types. The T_1 of pore fluid increases with an increased f, due to the frequency-dependent of ρ_{1S} for the pore fluids. The T_2* of pore fluids decrease due to the increased magnetic susceptibility and f. The reason is that the increased magnetic susceptibility, T_d, and f can lead to the enhanced $M_D(t)$, resulting in the left shift of T_2* distribution peak, decreased signal intensity and sparse contour lines of fluid signals.

5. Frequency conversion of 2D NMR-based petrophysical parameters

Porosity, T_{2LM}^*, and T_{1LM} are important petrophysical parameters in shale. The blind source separation technique was used to conduct T_1-T_2 and T_1-T_2* spectra to acquire corresponding source signals for fluid components (Fig. 8).

The T_1-T_2* spectra are taken as an example, different signals for organic matter, water, and oil are provided for various f. The results indicate that the T_1 values of organic matter and oil increase with the increased f, while the T_1 value of water slightly increases with the increased f. Unlike organic matter, oil is located in organic pores and influenced by dispersed phase effects, leading to a shortening T_2*. Water does not exhibit strong frequency-dependent but is significantly affected by IMFG, resulting in apparent dispersed phase, with no significant change in T_1 and a shortening T_2*. The results are consistent with the simulation results based on the T_1-T_2* relaxation theory.

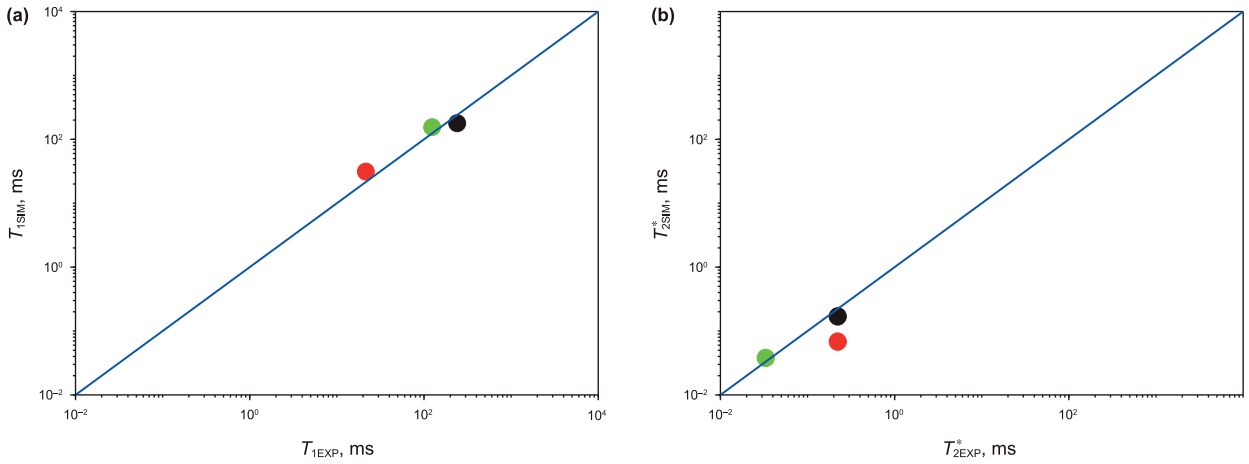

Fig. 4. Result comparison: **(a)** T_1, **(b)** T_2*.

5.1. Frequency conversion of porosity

(1) Pyrite contents

The pyrite content would affect the signal intensities and peak values of T_1-T_2 spectra and T_1-T_2* spectra for water and oil in Fig. 5, thereby influencing the porosity of each fluid component. Therefore, establishing the porosity conversion models for water and oil is necessary, as shown in Fig. 9. In Fig. 9, the black, purple, cyan, red, and blue lines are the variations of porosity with f. The blue, red, and green dashed lines are the boundaries of 200, 21.36, and 2 MHz, respectively. The results show that, for T_1-T_2 spectra and T_1-T_2* spectra, the porosity of water and oil decreases with the increased T_E, pyrite content, f, and T_d. Because their increases can lead to an increased relaxation rate of oil and water. The increased relaxation rate of water can occur due to the differences in the environments of water and oil, causing porosity of water to decrease more rapidly with f. Due to T_E being two orders of magnitude greater than T_d, the measured porosity from SR-CPMG is lower than that from the SR-FID pulse sequence. If the pyrite content is 5.43%, $T_d = 1$ μs, $T_E = 0.08$ ms, and $f = 200$ MHz, the T_1-T_2*-based water porosity is 1.735 times that of T_1-T_2-based water porosity. If $T_d = 2$ μs, $T_E = 0.2$ ms, T_1-T_2*-based water porosity is 1.70 times that of T_1-T_2-based water porosity. If $T_d = 4$ μs, $T_E = 0.4$ ms, the T_1-T_2*-based water porosity is 2.39 times that of T_1-T_2-based water porosity. Fig. 9 can be served T_1-T_2-based and T_1-T_2*-based porosity conversion cross-plots influenced by pyrite contents.

(2) Clay contents

The clay contents would affect the signal intensities and peaks values of T_1-T_2 spectra and T_1-T_2* spectra for water in Fig. 6, thereby influencing the porosity of various fluid components. Therefore, establishing porosity conversion models for water is necessary, as shown in Fig. 10. In the figure, the black, purple, cyan, red, and blue solid lines are the variations of porosity with f. The blue, red, and green dashed lines are the boundaries at magnetic field frequencies of 200, 21.36, and 2 MHz, respectively. The results indicate that for T_1-T_2 and T_1-T_2* spectra, the water-filled porosity decreases with increasing f, clay content, T_E, and T_d. As explained earlier, further elaboration is not necessary here. When $T_d = 1$ μs, $f = 200$ MHz, clay content is 16%, and $T_E = 0.08$ ms, the T_1-T_2*-based water-saturated porosity is 1.45 times that of T_1-T_2-based water-saturated. When $T_d = 2$ μs, $T_E = 0.2$ ms, the T_1-T_2*-based water-saturated porosity is 1.92 times that of T_1-T_2-based water-saturated porosity. When $T_d = 4$ μs, $T_E = 0.4$ ms, the T_1-T_2*-based water-saturated porosity is 1.59 times that of T_1-T_2-based water-saturated. Fig. 10 can be served T_1-T_2-based and T_1-T_2*-based porosity conversion cross-plots influenced by clay contents.

(3) Clay types

The results in Fig. 7 show the increased SDPM of clay minerals affects the peak values and signal intensities of T_1-T_2 and T_1-T_2* spectra for water, thereby influencing the porosity of various fluid components. Therefore, establishing a porosity conversion models for water at varying clay types is necessary, as shown in Fig. 11. In the figure, the solid blue and red lines represent the variation of porosity with f for varying clay minerals. The blue, red, and green dashed lines are the boundaries of 200, 21.36, and 2 MHz, respectively. The results show that, for T_1-T_2 and T_1-T_2* spectra, the water-saturated porosity decreases with the increased T_d, T_E, magnetic susceptibility and f. As explained earlier, it would not be reiterated here. When $f = 200$ MHz, $T_d = 1$ μs, $T_E = 0.08$ ms, and clay mineral is montmorillonite, the T_1-T_2*-based water-saturated porosity is 1.19 times that of T_1-T_2-based water-saturated. When $T_d = 2$ μs, $T_E = 0.2$ ms, the T_1-T_2*-based water-saturated is 1.85 times that of T_1-T_2-based water-saturated. When $T_d = 4$ μs, $T_E = 0.4$ ms, the T_1-T_2*-based water-saturated porosity is 2.05 times that of T_1-T_2*-based water-saturated porosity. Fig. 11 can be served as a T_1-T_2-based and T_1-T_2*-based porosity conversion cross-plots influenced by clay types.

5.2. Frequency conversion of T^*_{2LM} and T_{2LM}

Based on the T_1-T_2 and T_1-T_2* spectra, the corresponding T_1 distribution, T_2 distribution, and T_2* distribution can be calculated by longitudinal and transverse accumulations. The geometric mean can be calculated using the following Eq. (14), which can be expressed as:

$$\begin{cases} T_{1\mathrm{LM}} = \exp\left(\sum_i^{\mathrm{bin}} f_{i1}\ \ln(T_{1i}) \Big/ \sum_i^{\mathrm{bin}} f_{i1}\right) = \exp\left(\sum_i^{\mathrm{bin}} f_{i1}\ \ln(T_{1i}) \Big/ \mathrm{porosity}\right) \\ T_{2\mathrm{LM}} = \exp\left(\sum_i^{\mathrm{bin}} f_i\ \ln(T_{2i}) \Big/ \sum_i^{\mathrm{bin}} f_i\right) = \exp\left(\sum_i^{\mathrm{bin}} f_i\ \ln(T_{2i}) \Big/ \mathrm{porosity}\right) \\ T^*_{2\mathrm{LM}} = \exp\left(\sum_i^{\mathrm{bin}} f_i^*\ \ln(T^*_{2i}) \Big/ \sum_i^{\mathrm{bin}} f_i^*\right) = \exp\left(\sum_i^{\mathrm{bin}} f_i^*\ \ln(T^*_{2i}) \Big/ \mathrm{porosity}^*\right) \end{cases} \tag{14}$$

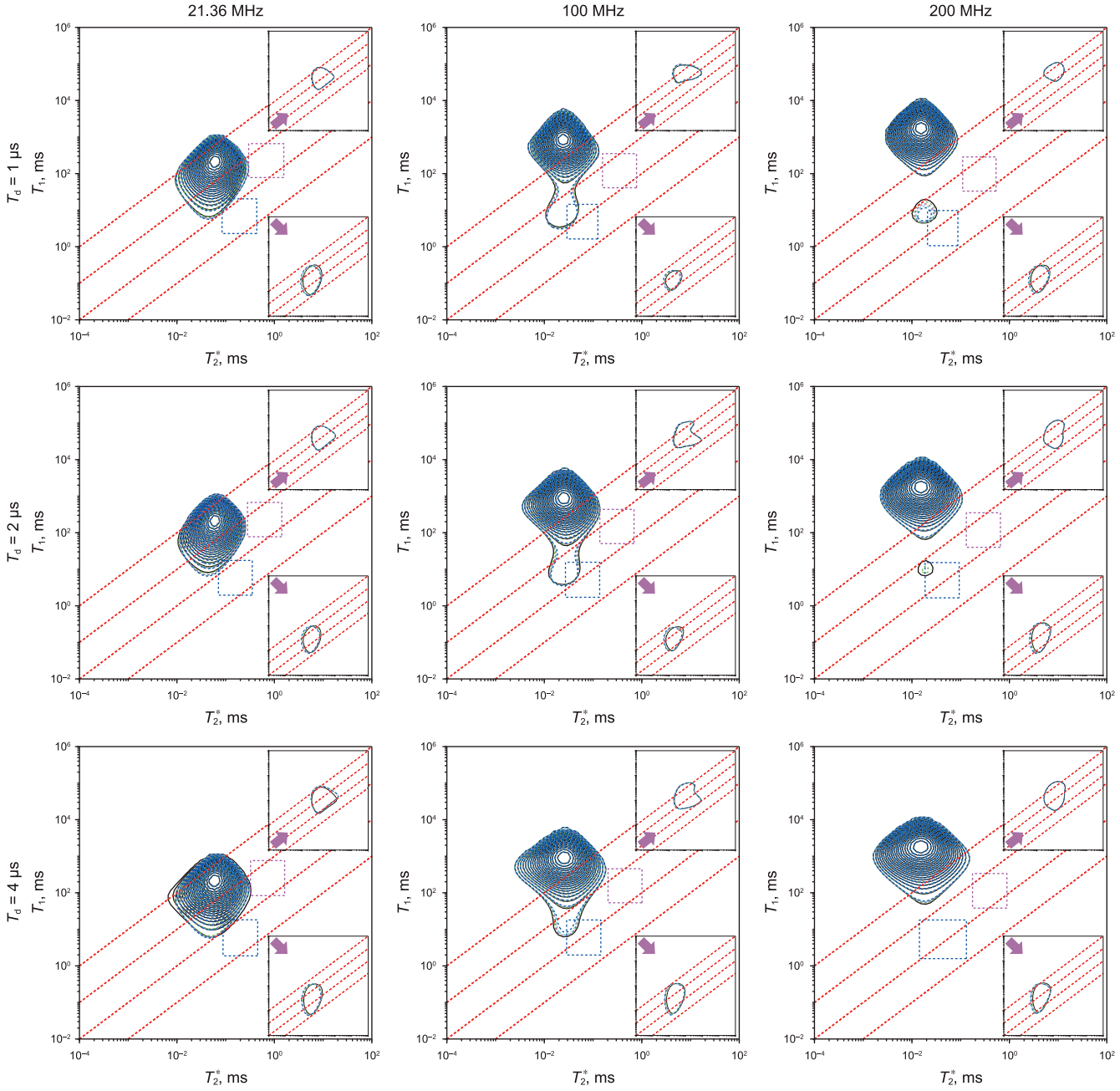

Fig. 5. T_1-T_2* spectra of all compositions with varying pyrite contents at different f and dwell times.

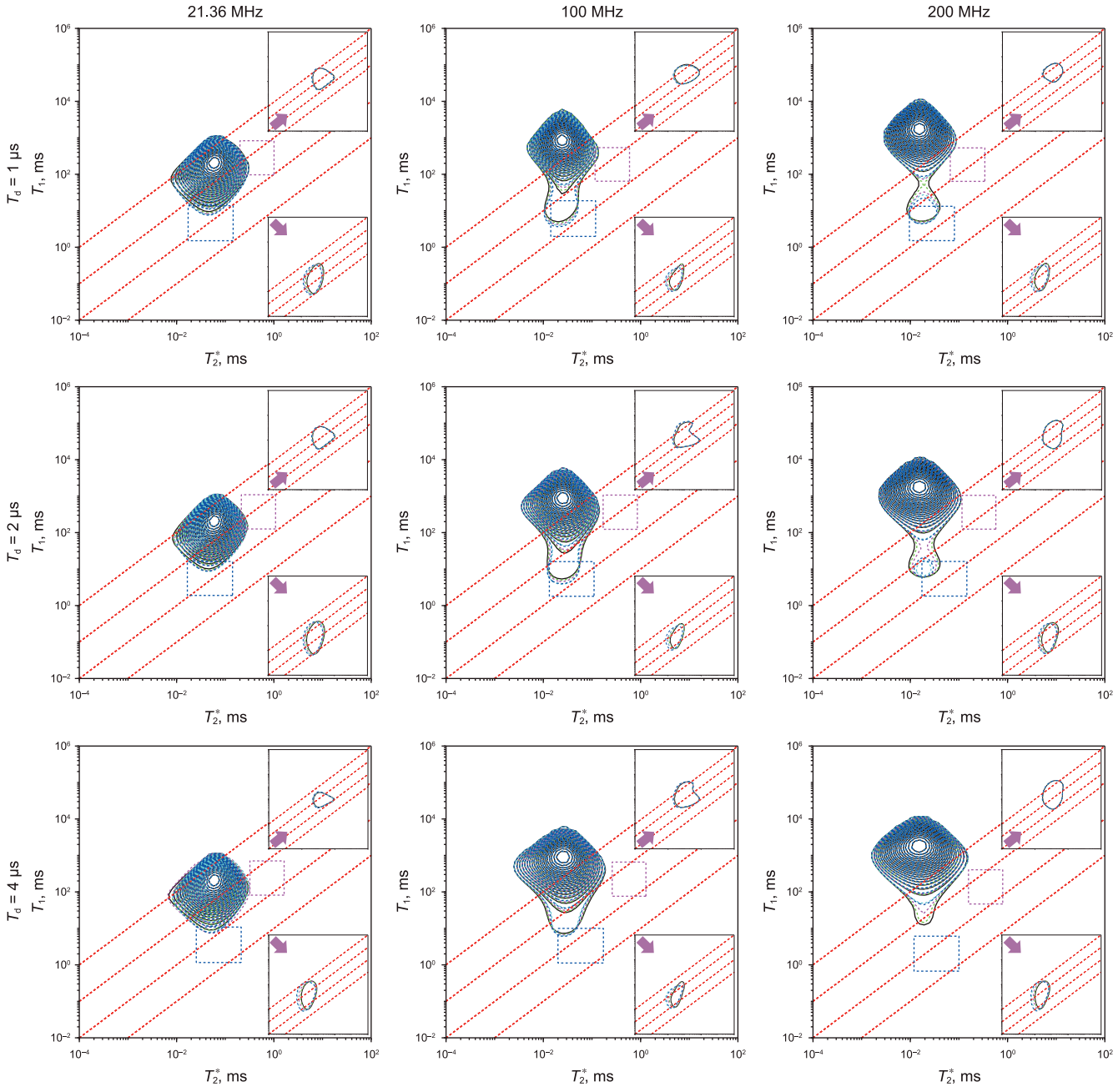

Fig. 6. T_1-T_2* spectra of all compositions with varying clay contents at different f and dwell times.

where, bin represents the number of points for T_1, T_2, or T_2* distribution. f_{i1}, f_i, and f_i^* represents the amplitude of T_1, T_2, T_2* distributions at the i-th point. porosity represents the porosity from cumulative T_1 or T_2 distribution. porosity* represents the porosity from cumulative T_2* distribution.

(1) Pyrite contents

The pyrite content affects signal intensities and the peaks of T_1-T_2 spectra and T_1-T_2* spectra for water and oil, thereby influencing T_{2LM} and T_{2LM}^*. Therefore, establishing the T_{2LM}^* conversion models for water and oil is necessary, as shown in Fig. 12. In the figure, the black, purple, cyan, red, and blue lines are the variations of T_{2LM} and T_{2LM}^* with f. The blue, red, and green dashed lines are the boundaries at magnetic field frequencies of 200, 21.36, and 2 MHz, respectively. The results indicate that the T_1-T_2 spectra and T_1-T_2* spectra are affected by both peak shifting and porosity reduction. According to Eq. (14), if peak shifting dominates, the value decreases, otherwise the value increases. Different plots in Fig. 12 represent the impact of pyrite content on T_{2LM} and T_{2LM}^*. When pyrite content is 5.43%, $f = 200$ MHz, $T_d = 1$ μs, $T_E = 0.08$ ms, and $T_{2LM}^* = 0.017$ ms, which is 0.012 times that of T_{2LM}. When pyrite content is 5.43%, $f = 200$ MHz, $T_d = 2$ μs, $T_E = 0.2$ ms, and T_{2LM}^* is 0.016 ms, which is 0.016 times that of T_{2LM}. When pyrite content is 5.43%, $f = 200$ MHz, $T_d = 4$ μs, $T_E = 0.4$ ms, and T_{2LM}^* is 0.015 ms, which is 0.015 times that of T_{2LM}. Fig. 12 can be served as the T_1-T_2*-based T_{2LM}^* and T_1-T_2-based T_{2LM} conversion cross-plots influenced by pyrite contents.

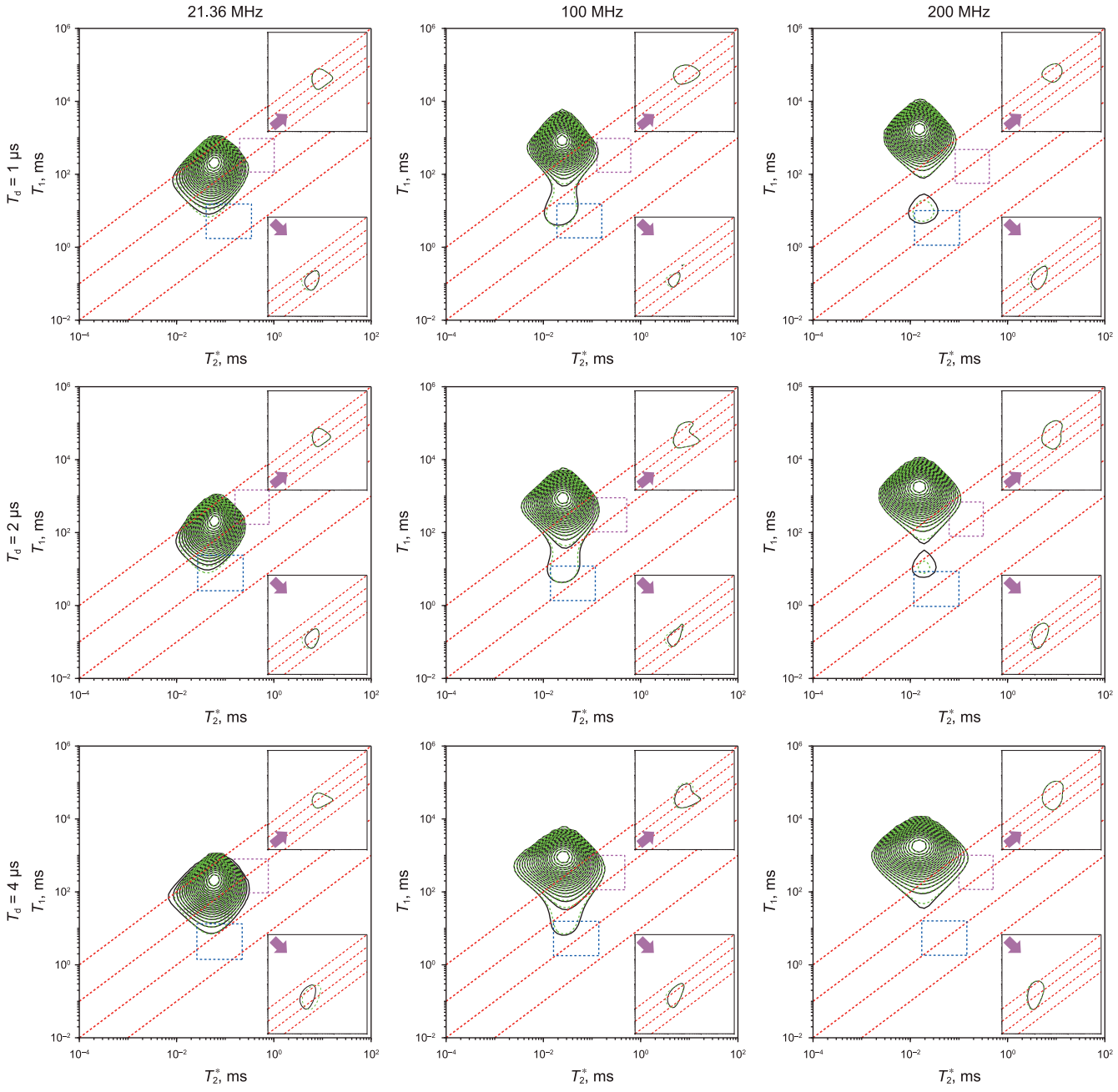

Fig. 7. T_1-T_2* spectra of all compositions with varying clay types at different f and dwell times.

(2) Clay contents

The results in Fig. 10 demonstrate that clay content affects the peak values and signal intensities of both T_1-T_2 and T_1-T_2* spectra of water, thereby influencing T_{2LM} and T^*_{2LM}. Hence, establishing the T_{2LM} or T^*_{2LM} conversion models for water is necessary influenced by clay minerals, as shown in Fig. 13. In the figure, in black, purple, cyan, red, and blue lines represent the changes of T_{2LM} and T^*_{2LM} with f. The blue, red, and green dashed lines are boundaries of 200, 21.36, and 2 MHz. The results indicate that both spectrum peak shifting and porosity reduction jointly affect T_{2LM} and T^*_{2LM}. According to Eq. (14), if spectrum peak shifting predominates, T_{2LM} and T^*_{2LM} decreases, othwewise T_{2LM} and T^*_{2LM} increases. Different panels in Fig. 13 illustrate the impacts of clay content on T_{2LM} and T^*_{2LM}. If clay content is 16%, T_E = 0.08 ms, T_d = 1 μs, and the f is 200 MHz, the T^*_{2LM} is 0.019 ms, which is 0.014 times that of T_{2LM}. If T_E = 0.2 ms, and T_d = 2 μs, T^*_{2LM} is 0.018 ms, which is 0.02 times that of T_{2LM}. If T_E = 0.4 ms, and T_d = 4 μs, T^*_{2LM} = 0.188 ms, which is 0.024 times that of T_{2LM}. From Fig. 13, the effects of clay content on T^*_{2LM} and T_{2LM} are minimal, because the increased clay content can reduce the peak and porosity to the same extent, they have change little. Fig. 13 can be served as the T_1-T_2-based T_{2LM} and T_1-T_2*-based T^*_{2LM} conversion cross-plots influenced by clay contents.

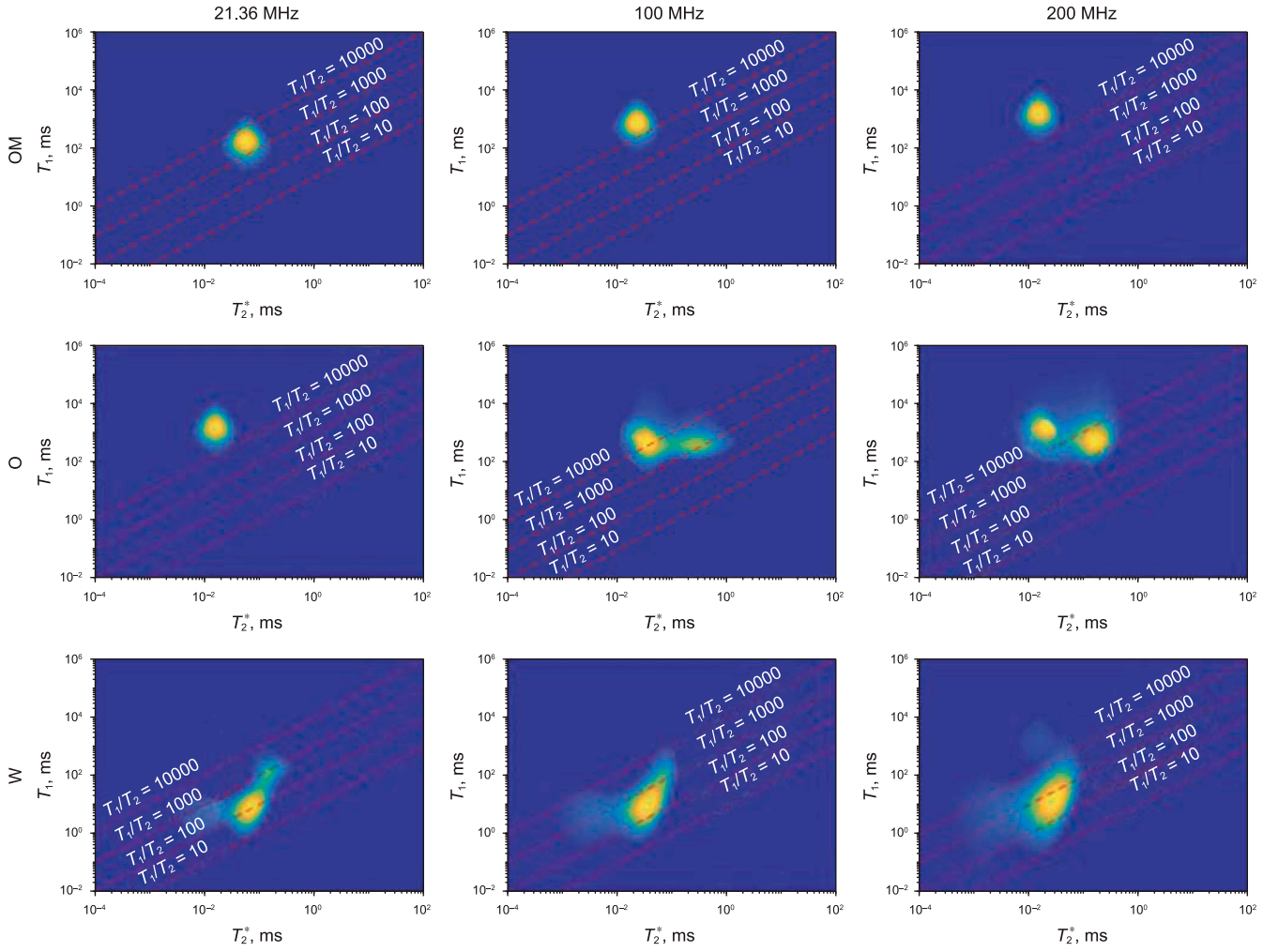

Fig. 8. T_1-T_2* spectra of organic matter, oil, and water by blind source separation at different *f*. O and W represent the oil and water, respectively.

(3) Clay types

The results in Fig. 11 show different clay types affect the peak values and signal intensities of T_1-T_2 spectra and T_1-T_2* spectra for water, thereby influencing T_{2LM} or T_{2LM}^*. Therefore, establishing the T_{2LM} or T_{2LM}^* conversion models for water influenced by clay types is necessary, as shown in Fig. 14. In the figure, the red and blue lines are the changes of T_{2LM} and T_{2LM}^* with *f*. The blue, red, and green dashed lines in the figure are the boundaries of 200, 21.36, and 2 MHz, respectively. The results indicate that for T_1-T_2 spectra and T_1-T_2* spectra, the T_{2LM} or T_{2LM}^* are simultaneously affected by peak shift and porosity reduction. According to Eq. (14), if peak shift dominates, T_{2LM} or T_{2LM}^* decreases, otherwise T_{2LM} or T_{2LM}^* increases. Fig. 14 depicts the influence of different clay types on T_{2LM} and T_{2LM}^*. Fig. 14 can be served as the T_{2LM} and T_{2LM}^* conversion models for the influence by clay types.

5.3. Frequency conversion of T_{1LM}

(1) Pyrite contents

The numerical simulations in Fig. 9 demonstrate that varying pyrite content affects the peak positions and signal intensities of water and oil for T_1-T_2 or T_1-T_2* spectra, thereby influencing T_{1LM}. Consequently, establishing T_{1LM} conversion models for water and oil is necessary, as shown in Fig. 15. In the figure, black, purple, cyan, red, and blue lines are the variation of T_{1LM} with *f* for varying pyrite contents. blue, red, and green dashed lines depict boundaries at magnetic field frequencies of 200, 21.36, and 2 MHz, respectively. The results show that, for T_1-T_2 and T_1-T_2* spectra, as T_E and T_d increase, relaxation rates intensify. Consequently, the cumulative T_2 and T_2* distributions derived from these spectra shift to the left, indicating a decreased porosity. Given the unchanged regularization parameter for inversion, the amplitude of the cumulative T_1 distribution decreases due to the influence of cumulative T_2* distribution, resulting in the decreased porosity. When the pyrite content is 5.43%, $T_d = 1$ μs, $T_E = 0.08$ ms, and the $f = 200$ MHz, the T_1-T_2*-based T_{1LM}^* is 4.329 ms, which is 0.8 times that of T_1-T_2-based T_{1LM}. When $T_d = 2$ μs, and $T_E = 0.2$ ms, the T_1-T_2*-based T_{1LM}^* is 5.47 ms, which is 0.793 times that of the T_1-T_2 -based T_{1LM}. Similarly, when $T_d = 4$ μs, and $T_E = 0.4$ ms, the T_1-T_2*-based T_{1LM}^* is 8.84 ms, which is 0.63 times that of T_1-T_2-based T_{1LM}. Fig. 15 can be served as the T_1-T_2-based and T_1-T_2*-based conversion cross-plots influenced by pyrite contents.

(2) Clay contents

The results in Fig. 10 show different clay contents affect the peak values and signal intensities of T_1-T_2 and T_1-T_2* spectra for

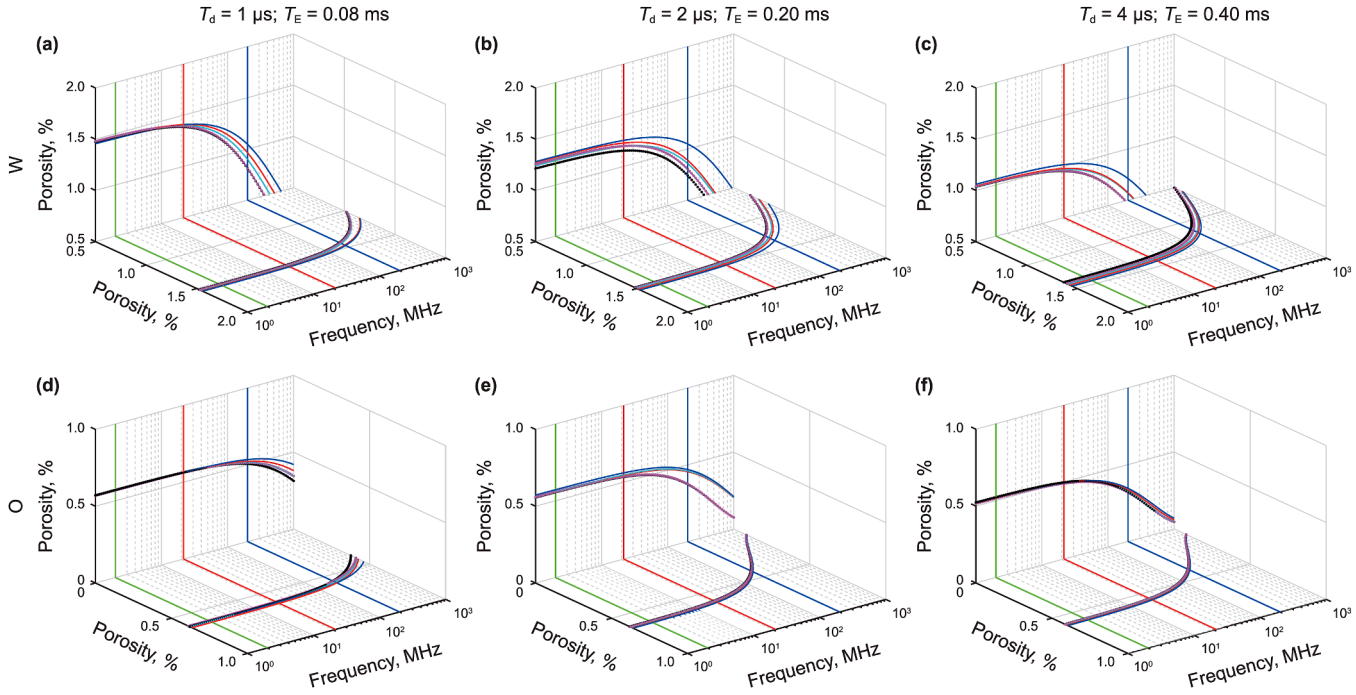

Fig. 9. Porosity frequency conversions based on T_1-T_2 and T_1-T_2* for different pyrite contents and echo spacings (or dwell times).

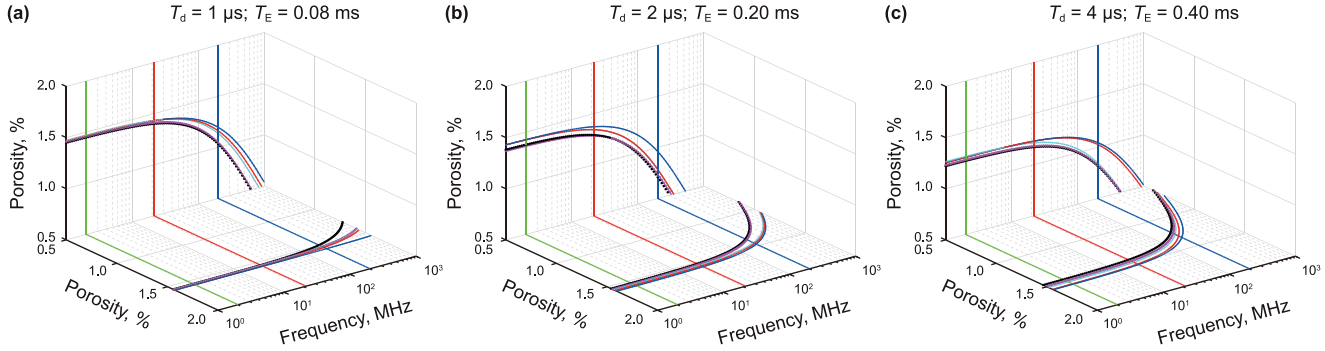

Fig. 10. Porosity frequency conversions based on T_1-T_2 and T_1-T_2* for different clay contents and echo spacings (or dwell times).

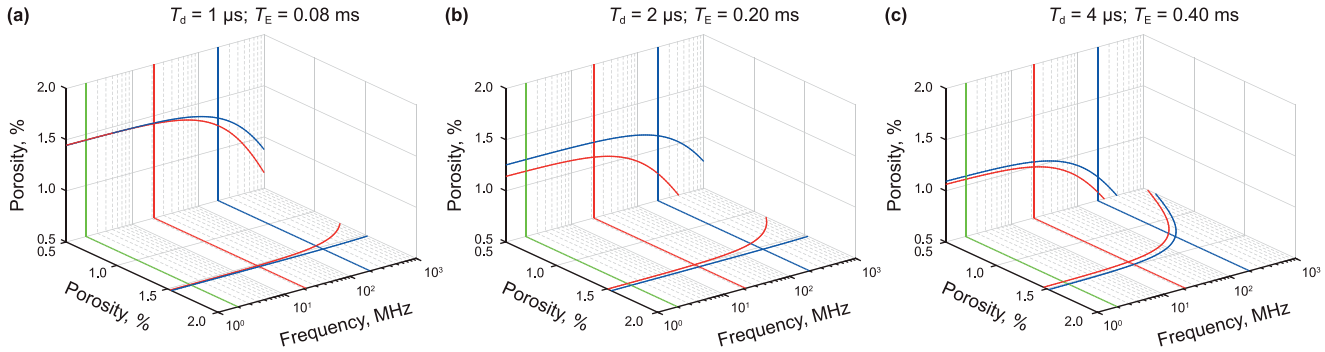

Fig. 11. Porosity frequency conversions based on T_1-T_2 and T_1-T_2* for different clay types and echo spacings (or dwell times).

water, thereby influencing T_{1LM}. Therefore, establishing the T_{1LM} conversion models on water influenced by clay minerals is necessary, as shown in Fig. 16. In the figure, black, purple, cyan, red, and blue lines are the variation of T_{1LM} with f. The blue, red, and green dashed lines in the figure are boundaries of 200, 21.36, and 2 MHz, respectively. The results show that for T_1-T_2 and T_1-T_2* spectra, the relaxation rates increase with increasing T_E and T_d. T_{1LM} are affected, and the details are omitted here. If $T_E = 0.08$ ms, $T_d = 1$ μs, and $T_d = 2$ μs, $T_E = 0.2$ ms, determined by porosity, T_{1LM} increase according to Eq. (14). When $T_d = 4$ μs, $T_E = 0.4$ ms, T_{1LM}

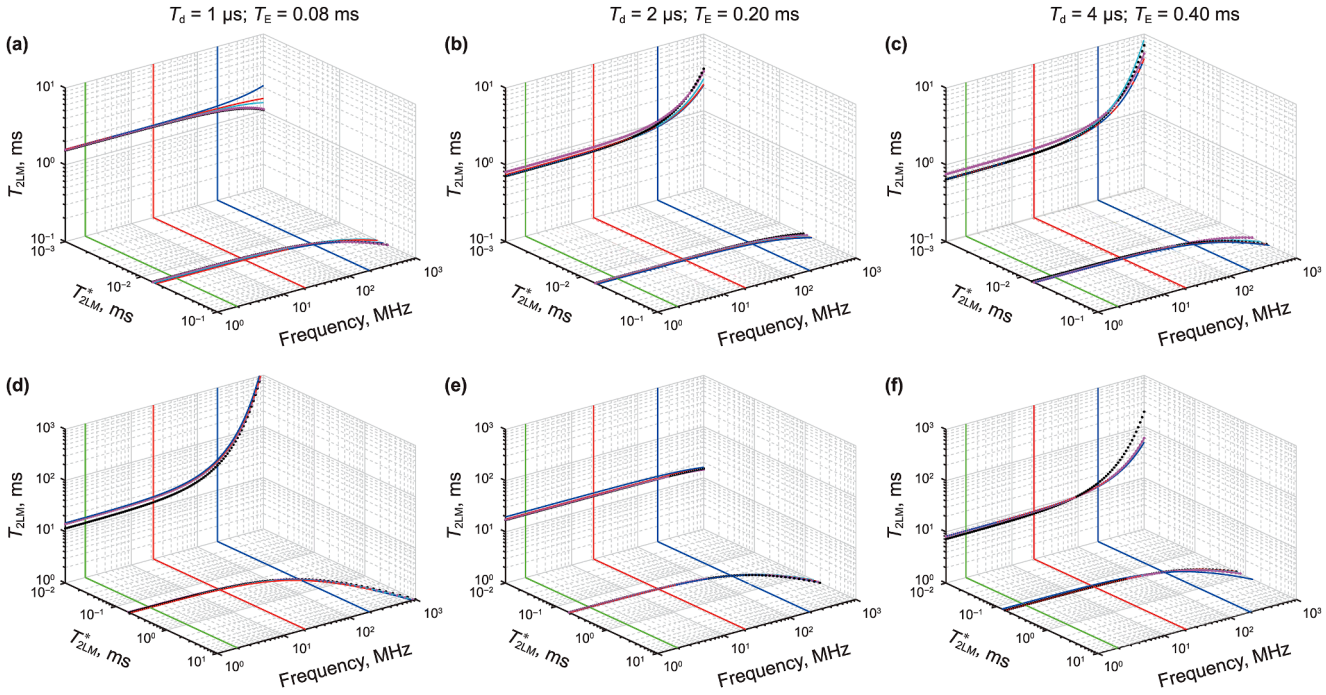

Fig. 12. Frequency conversions of T_{2LM} and T^*_{2LM} based on T_1-T_2 and T_1-T_2* for different pyrite contents and echo spacings (or dwell times).

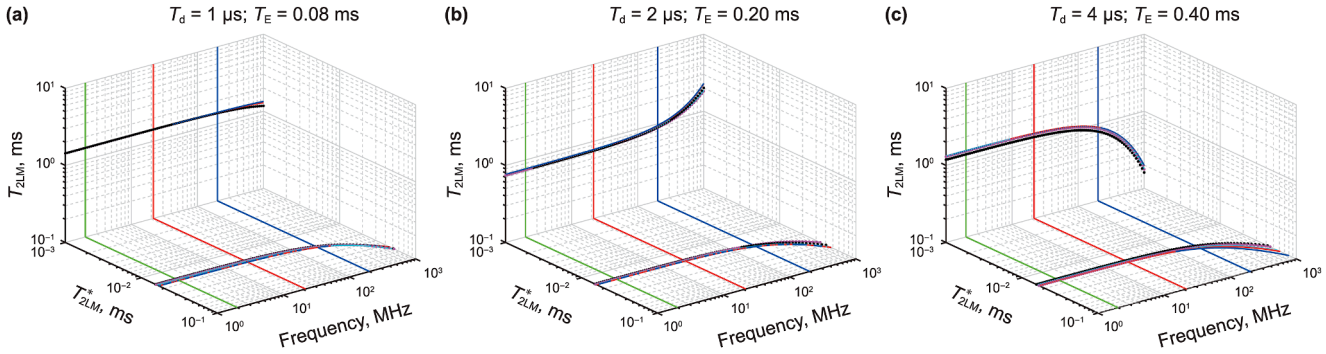

Fig. 13. Frequency conversions of T_{2LM} and T^*_{2LM} based on T_1-T_2 and T_1-T_2* for different clay contents and echo spacings (or dwell times).

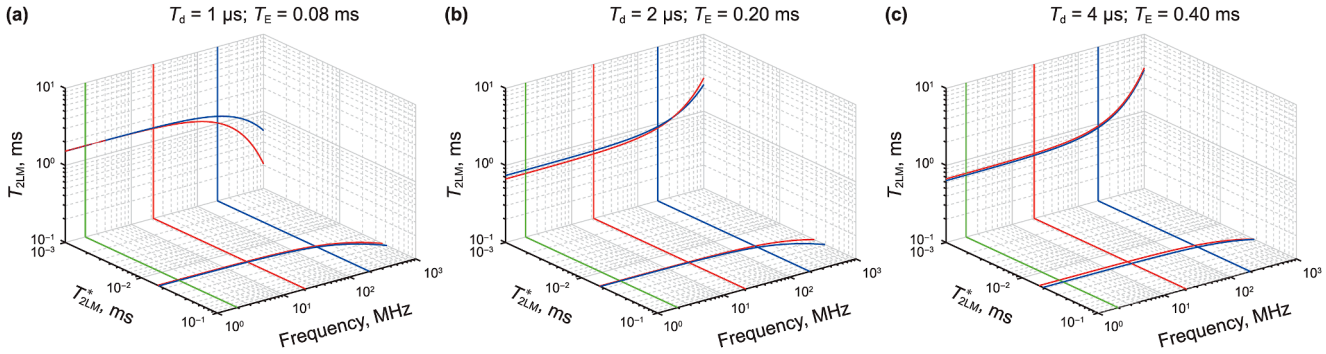

Fig. 14. Frequency conversions of T_{2LM} and T^*_{2LM} based on T_1-T_2 and T_1-T_2* for different clay types and echo spacings (or dwell times).

values decrease based on the degree of amplitude reduction. The increasing f and clay content enhance relaxation rates. T_{1LM} are affected, and the details are omitted here. When T_E = 0.08 ms, T_d = 1 μs, the clay content is 16%, and the f is 200 MHz, the T_1-T_2*-based T_{1LM} is 4.92 ms, which is 0.5 times that of the T_1-T_2-based T_{1LM}. When T_d = 2 μs and T_E = 0.2 ms, the T_1-T_2*-based T_{1LM} is 4.97 ms, which is 0.41 times that of the T_1-T_2-based T_{1LM}. Similarly, T_d = 4 μs and T_E = 0.4 ms, the T_1-T_2*-based T_{1LM} is 6.71 ms, which is

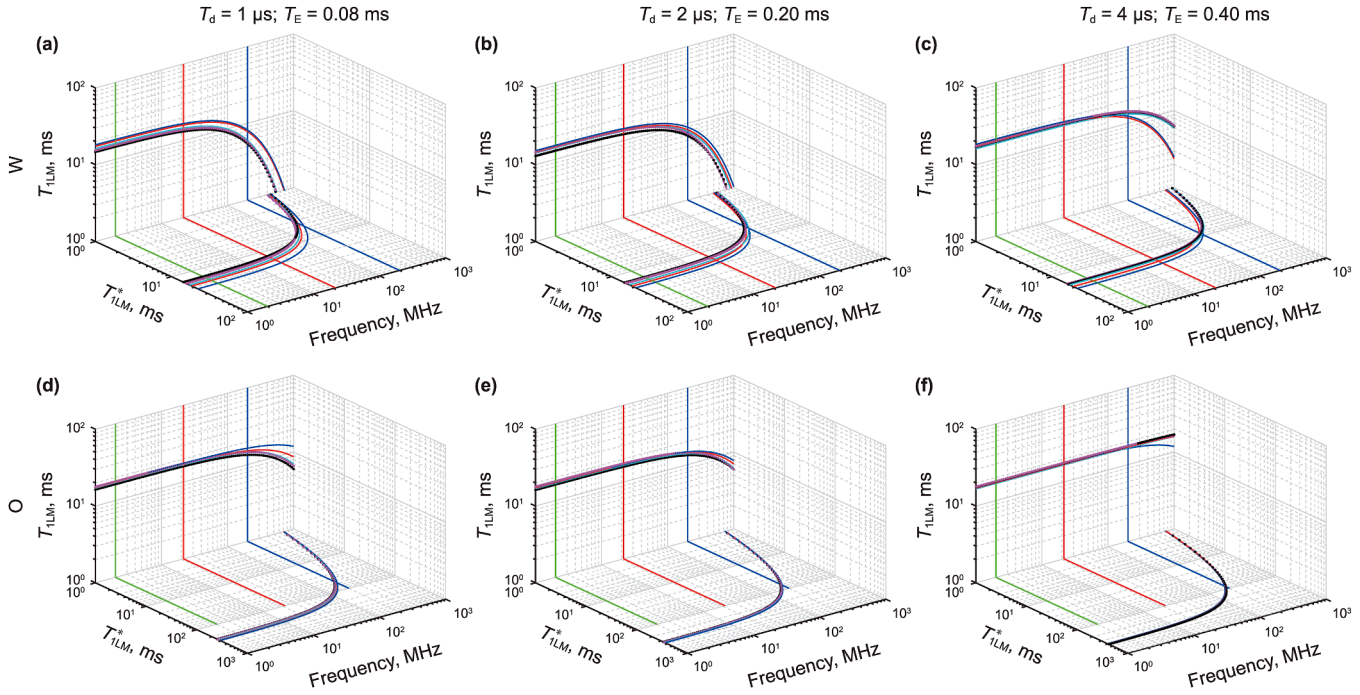

Fig. 15. T_{1LM}-Frequency conversions based on T_1-T_2 and T_1-T_2* for different pyrite contents and echo spacings (or dwell times).

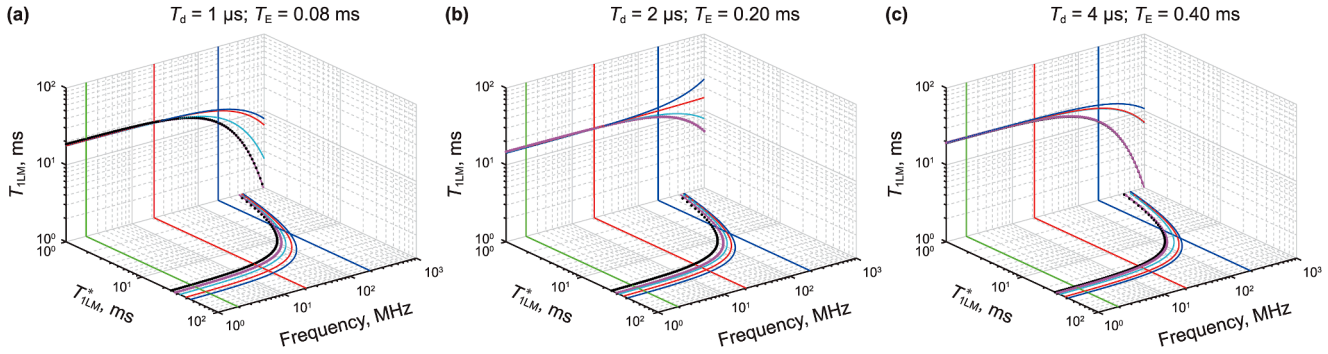

Fig. 16. T_{1LM}-Frequency conversions based on T_1-T_2 and T_1-T_2* for different clay contents and echo spacings (or dwell times).

0.63 times that of T_1-T_2-based T_{1LM}. Fig. 16 can be served as the T_1-T_2-based and T_1-T_2*-based T_{1LM} conversion cross-plots influenced by clay contents.

(3) Clay types

The results in Fig. 11 show different clay types affect the peak values and signal intensities of T_1-T_2 and T_1-T_2* spectra for water, thereby influencing T_{1LM}. Therefore, establishing the T_{1LM} conversion models for water influenced by clay minerals is necessary, as shown in Fig. 17. In the figure, the black, purple, cyan, red, and blue solid lines represent the variations of T_{1LM} with f. The blue, red, and green dashed lines in the figure are the boundaries of 200, 21.36, and 2 MHz, respectively. The results show that, for both T_1-T_2 and T_1-T_2* spectra, the relaxation rates increase with the increased T_E and T_d, T_{1LM} is influenced by them. When f is 200 MHz, determined by the porosity (Fig. 17(a)), as f and magnetic susceptibility increase, the relaxation rates enhance to affect the T_{1LM}. When T_E is 0.4 ms or T_d is 4 μs, T_{1LM} is determined by porosity and they increase (Fig. 17(c)). Additionally, T_{1LM} is determined by the extent of amplitude reduction and decreases (Fig. 17(a)–(b)). When T_d = 1 μs, T_E = 0.08 ms, clay content is 16%, and the f is 200 MHz, T_1-T_2*-based T_{1LM} is 4.72 ms, which is 0.62 times that of T_1-T_2-based T_{1LM}. When T_d = 2 μs and T_E = 0.2 ms, T_1-T_2*-based T_{1LM} is 8.99 ms, 1.025 times the T_1-T_2-based T_{1LM}. Similarly, when T_d = 4 μs and T_E = 0.4 ms, T_1-T_2*-based T_{1LM} is 13.31 ms, which is 0.92 times that of T_1-T_2-based T_{1LM}. Fig. 17 can be served as the T_1-T_2*-based and T_1-T_2-based T_{1LM} conversion cross-plots influenced by clay contents.

6. Discussion

In the shale sample, the organic matter content, the porosity of organic pore oil and inorganic pore water are 22.36%, 0.55%, and 1.39%, respectively. The organic matter content is an order of magnitude higher than the pore fluids. In the T_1-T_2* spectra, the signal intensity from organic matter is higher compared to pore fluids. As the T_E increases, the signal intensity from organic matter decreases, but it remains stronger than that from pore fluids. In actual shale oil reservoir, organic matter content is lower than

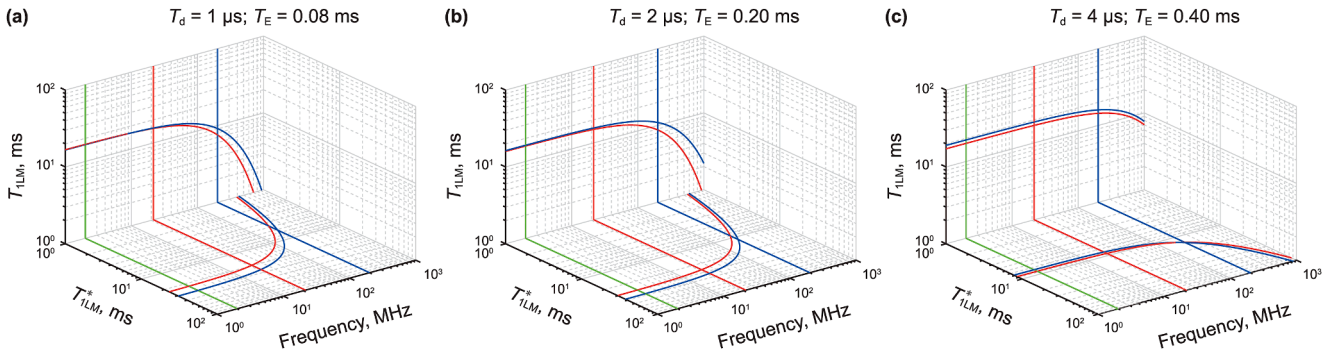

Fig. 17. T_{1LM}-Frequency conversions based on T_1-T_2 and T_1-T_2* for different clay types and echo spacings (or dwell times).

organic pore oil and inorganic pore water porosity. In the T_1-T_2* spectra, the signal intensity from pore fluids is stronger. As T_E increased, the signal intensity of organic matter decreases, indicating weaker signal intensity. Nevertheless, the proposed T_1-T_2* relaxation theory and simulation method can still quantify the impacts of heterogeneous mineral distributions. The extracted petrophysical parameters through numerical simulations can be normalized to help mitigate the influence of mineral contents and types on T_1-T_2* responses. By comparing the simulation results between T_1-T_2* and T_1-T_2 for shale oil reservoirs with complex mineral compositions, we can establish the frequency conversion relationships of fluid component contents on NMR laboratory measurements (T_1-T_2* spectra) and NMR logging (T_1-T_2 spectra). It can further unlock the potential reserve of shale oil reservoirs and contribute to reserve growth and production enhancement in such reservoirs. In future work, we will further study how wettability and occurrence states of fluids affect NMR responses, to gain deep insights into NMR response mechanisms in shale oil reservoirs.

7. Conclusions

Accurate characterization of petrophysical properties contributes significantly to shale oil reserve assessments. The complex mineral compositions, heterogeneous organic matter distributions, and differences between downhole NMR logging and laboratory NMR measurement pose challenges to the petrophysical characterization by 2D NMR technique. Therefore, we explored the variation law of petrophysical parameters such as porosity at different f using low-cost numerical simulation techniques that reflect single-factor influences. The T_1-T_2* numerical simulations in shale oil reservoir were firstly proposed in this paper. On the basis of the RW algorithm, the impacts from pyrite content, differences in f, clay types and contents on T_1-T_2* responses were firstly investigated in shale oil reservoir, revealing the NMR response mechanisms in shale oil reservoir with complex mineral compositions at different f. The T_1-T_2*-based petrophysical conversion relationships were established, and the main conclusions are as follows:

(1) FIB-SEM experiments representing the microscale, QEMSCAN experiments, XRD experiments, and multi-temperature-stage pyrolysis experiments at the macroscale were combined to construct the multi-component digital shale cores representing shale reservoirs. The parallel experiments including different frequency T_2 experiments, T_2* experiments, and T_1-T_2 experiments provided accurate numerical simulation parameters for T_1-T_2* simulations. The accuracy of the proposed T_1-T_2* relaxation theory and numerical simulation methods can be validated.

(2) T_1-T_2* numerical simulations indicate that the instrument acquisition parameter T_d should be minimized. The f, pyrite content, and clay can influence the T_1-T_2* responses, with a greater impact on inorganic pore water. Pyrite has a larger effect on porosity than that of clay. Due to the T_E being two orders of magnitude larger than the T_d, the T_1-T_2*-based porosity is higher compared to T_1-T_2-based porosity. When pyrite content is 5.43%, T_d = 4 μs, T_E = 0.4 ms, and f is 200 MHz, the T_1-T_2*-based porosity is 2.39 times that of the T_1-T_2*-based porosity. As f increases, the influences of clay content and type, pyrite content on T^*_{2LM} inorganic pore water increase. When pyrite content is 5.43%, T_d = 4 μs, T_E = 0.4 ms, and f is 200 MHz, the T^*_{2LM} is 0.015 ms, which is 0.015 times that of T_{2LM}. When f increased, relaxation rates strengthen, determined by the spectral peak shift of T_2* distribution, the T^*_{2LM} decreases. The T_d = 4 μs, T_E = 0.4 ms, T_{1LM} is 8.84 ms, which is 0.63 times that of T_{1LM}.

(3) T_{2LM}, T^*_{2LM}, T_{1LM}, and porosity are influenced by the complex minerals. The petrophysical conversion models can be achieved based on T_1-T_2* numerical simulations.

The T_1-T_2* relaxation theory was proposed in this paper, which establishes the foundation for frequency conversion relationships of petrophysical parameters between NMR laboratory measurements (T_1-T_2* spectra) and NMR logging (T_1-T_2 spectra). It can further unlock the potential reserve of shale oil reservoirs and contribute to reserve growth and production enhancement in such reservoirs. It is also crucial for CO_2 sequestration capacity evaluation in shale oil reservoirs.

CRediT authorship contribution statement

Ji-Long Liu: Writing – original draft, Validation, Resources, Investigation, Data curation, Visualization, Software, Methodology, Formal analysis, Conceptualization. **Ran-Hong Xie:** Writing – review & editing, Project administration, Supervision, Funding acquisition. **Jiang-Feng Guo:** Visualization, Writing – review & editing, Resources. **Chen-Yu Xu and Guo-Wen Jin:** Conceptualization. **Xiang-Yu Wang, Bo-Chuan Jin, and Xiao-Long Ju:** Data Curation.

Declaration of competing interest

The authors declare that they have no known competing financial interests or personal relationships that could have appeared to influence the work reported in this paper.

Acknowledgements

This work was funded by the National Natural Science Foundation of China (42174131).

List of abbreviations

2D NMR	Two-dimensional nuclear magnetic resonance
f	Magnetic field frequency
IMFs	Internal magnetic fields
EMF	External magnetic fields
SDPM	Susceptibility differences between the pore fluid and the matrix
FID	Free induction decay
RW	Random walk
T_{2B}	Bulk relaxation time
O	Oil
W	Water
SR-FID	Saturation recovery-free induction decay
XRD	X-ray diffraction quantitative analysis
QEMSCAN	Quantitative evaluation of minerals by scanning electron microscopy
FIB-SEM	Focused ion beam scanning electron microscopy
IR-CPMG	Inversion recovery - Carr-Purcell-Meiboom-Gill

References

Audoly, B., Sen, P.N., Ryu, S., et al., 2003. Correlation functions for inhomogeneous magnetic field in random media with application to a dense random pack of spheres. J. Magn. Reson. 164 (1), 154–159. https://doi.org/10.1016/S1090-7807(03)00179-4.

Bai, M., Sun, J., Song, K., et al., 2015. Evaluation of mechanical well integrity during CO_2 621 underground storage. Environ. Earth Sci. 73, 6815–6825. https://doi.org/10.1007/s12665-015-622.4157-5.

Bergman, D.J., Dunn, K.J., 1995. NMR of diffusing atoms in a periodic porous medium in the presence of a nonuniform magnetic field. Phys. Rev. 52 (6), 6516. https://doi.org/10.1103/PhysRevE.52.6516.

Bloembergen, N., Purcell, E.M., Pound, R.V., 1948. Relaxation effects in nuclear magnetic resonance absorption. Phys. Rev. 73 (7), 679. https://doi.org/10.1103/PhysRev.73.679.

Brown, R.J.S., Fantazzini, P., 1993. Conditions for initial quasilinear T_2^{-1} versus τ for carr-purcell-meiboom-gill NMR with diffusion and susceptibility differences in porous media and tissues. Phys. Rev. B 47 (22), 14823. https://doi.org/10.1103/PhysRevB.47.14823.

Butler, J.P., Reeds, J.A., Dawson, S.V., 1981. Estimating solutions of first kind integral equations with nonnegative constraints and optimal smoothing. SIAM J. Numer. Anal. 18, 381–397. https://doi.org/10.1137/0718025.

Chen, Q., Marble, A.E., Colpitts, B.G., et al., 2005. The internal magnetic field distribution, and single exponential magnetic resonance free induction decay, in rocks. J. Magn. Reson. 175 (2), 300–308. https://doi.org/10.1016/j.jmr.2005.05.001.

Cui, D., Yin, H., Liu, Y., et al., 2022. Effect of final pyrolysis temperature on the composition and structure of shale oil: synergistic use of multiple analysis and testing methods. Energy 252, 124062. https://doi.org/10.1016/j.energy.2022.124062.

Drain, L.E., 1962. The broadening of magnetic resonance lines due to field inhomogeneities in powdered samples. Proc. Phys. Soc. 80 (6), 1380–1382. https://doi.org/10.1088/0370-1328/80/6/119.

Ershadnia, R., Wallace, C.D., Hajirezaie, S., et al., 2022. Hydro-thermo-chemo-mechanical modeling of carbon dioxide injection in fluvial heterogeneous aquifers. Chem. Eng. J. 431, 133451. https://doi.org/10.1016/j.cej.2021.133451.657.

Ford, J.C., Wehrli, F.W., Chung, H.W., 1993. Magnetic field distribution in models of trabecular bone. Magn. Reson. Med. 30 (3), 373–379. https://doi.org/10.1002/mrm.1910300316.

Grunewald, E., Knight, R., 2011. The effect of pore size and magnetic susceptibility on the surface NMR relaxation parameter. Near Surf. Geophys. 9 (2), 169–178. https://doi.org/10.3997/1873-0604.2010062.

Guo, J.F., MacMillan, B., Zamiri, M.S., et al., 2021. Magnetic resonance T_1–T_2* and $T_{1\rho}$–T_2* relaxation correlation measurements in solid-like materials with non-exponential decays. J. Magn. Reson. 328, 107005. https://doi.org/10.1016/j.jmr.2021.107005.

Guo, J.F., Zamiri, M.S., Balcom, B.J., 2022a. Rapid measurement of T_1*–T_2* relaxation correlation with a look-Locker sequence. J. Magn. Reson. 335, 107123. https://doi.org/10.1016/j.jmr.2021.107123.

Guo, J.F., Zamiri, M.S., Balcom, B.J., 2022b. Optimization of two-dimensional T_1*–T_2* relaxation correlation measurements in shale. J. Petrol. Sci. Eng. 217, 110939. https://doi.org/10.1016/j.petrol.2022.110939.

Jiang, H., Liu, S., Wang, J., et al., 2023. Study on evolution mechanism of the pyrolysis of chang 7 oil shale from Ordos Basin in China. Energy 272, 127097. https://doi.org/10.1016/j.energy.2023.127097.

Kang, Z., Zhao, Y., Yang, D., 2020. Review of oil shale in-situ conversion technology. Appl. Energy 269, 115121. https://doi.org/10.1016/j.apenergy.2020.115121.

Lei, J., Pan, B., Guo, Y., et al., 2021. A comprehensive analysis of the pyrolysis effects on oil shale pore structures at multiscale using different measurement methods. Energy 227, 120359. https://doi.org/10.1016/j.energy.2021.120359.

Leung, D.Y.C., Caramanna, G., Maroto-Valer, M.M., 2014. An overview of current status of carbon dioxide. Renew. Sustain. Energy Rev. 39, 426–430. https://doi.org/10.1016/j.rser.2014.07.093.

Li, J., Wang, M., Jiang, C., et al., 2022. Sorption model of lacustrine shale oil: Insights from the contribution of organic matter and clay minerals. Energy 260, 125011. https://doi.org/10.1016/j.energy.2022.125011.

Lipari, G., Szabo, A., 1982. Model-free approach to the interpretation of nuclear magnetic resonance relaxation in macromolecules. 1. Theory and range of validity. J. Am. Chem. Soc. 104 (17), 4546–4559. https://doi.org/10.1021/ja00381a009.

Liu, Y., Rui, Z., Yang, T., et al., 2022a. Using propanol as an additive to CO_2 for improving CO_2 utilization and storage in oil reservoirs. Appl. Energy 311, 118640. https://doi.org/10.1016/j.apenergy.2022.118640.

Liu, J.L., Xie, R.H., Guo, J.F., et al., 2023. Multicomponent digital core construction and three-dimensional micro-pore structure characterization of shale. Phys. Fluids 35, 082003. https://doi.org/10.1063/5.0155425.

Liu, J.L., Xie, R.H., Guo, J.F., et al., 2024a. Study of nuclear magnetic resonance response mechanism in shale oil and correction of petrophysical parameters. Fuel 358, 130162. https://doi.org/10.1016/j.fuel.2023.130162.

Liu, J.L., Xie, R.H., Guo, J.F., 2024b. Pore-scale T_2-based numerical investigation on dynamics and wettability in mixed-wet shale oil reservoirs. Phys. Fluids 36, 122025. https://doi.org/10.1063/5.0247232.

Liu, J.L., Xie, R.H., Guo, J.F., 2024c. Numerical investigation of T_2^*-based and T_2-based petrophysical parameters frequency-dependent in shale oil. Energy 313, 133788. https://doi.org/10.1016/j.energy.2024.133788.

Liu, J.L., Xie, R.H., Guo, J.F., et al., 2025. Numerical investigation on 2-D NMR response mechanisms and the frequency conversion of petrophysical parameters in shale oil reservoirs. Pet. Sci. 22 (5), 1959–1976. https://doi.org/10.1016/j.petsci.2025.03.014.

Liu, J., Yang, Y., Sun, S., et al., 2022b. Flow behaviors of shale oil in kerogen slit by molecular dynamics simulation. Chem. Eng. J. 434, 134682. https://doi.org/10.1016/j.cej.2022.134682.

Müller, M., Kooman, S., Yaramanci, U., 2005. Nuclear magnetic resonance (NMR) properties of unconsolidated sediments in field and laboratory. Near Surf. Geophys. 3 (4), 275–285. https://doi.org/10.3997/1873-0604.2005023.

Müller-Petke, M., Hiller, T., Herrmann, R., et al., 2011. Reliability and limitations of surface NMR assessed by comparison to borehole NMR. Near Surf. Geophys. 9 (2), 123–134. https://doi.org/10.3997/1873-0604.2010066.

Ozotta, O., Kolawole, O., Malki, M.L., et al., 2022. Nano-to macro-scale structural, mineralogical, and mechanical alterations in a shale reservoir induced by exposure to supercritical CO_2. Appl. Energy 326, 120051. https://doi.org/10.1016/j.apenergy.2022.120051.

Saif, T., Lin, Q., Gao, Y., et al., 2019. 4D in situ synchrotron X-ray tomographic microscopy and laser-based heating study of oil shale pyrolysis. Appl. Energy 235, 1468–1475. https://doi.org/10.1016/j.apenergy.2018.11.044.

Sen, P.N., Axelrod, S., 1999. Inhomogeneity in local magnetic field due to susceptibility contrast. J. Appl. Phys. 86 (8), 4548–4554. https://doi.org/10.1063/1.371401.

Singer, P.M., Valiya, Parambathu, A., Wang, X., et al., 2020. Elucidating the ^{1}H NMR relaxation mechanism in polydisperse polymers and bitumen using measurements, MD simulations, and models. J. Phys. Chem. B 124 (20), 4222–4233. https://doi.org/10.1021/acs.jpcb.0c01941.

Tandon, S., Heidari, Z., Matenoglou, G., 2017. Pore-scale numerical modeling of nuclear magnetic resonance response in rocks with complex pore structure using finite volume method. In: SPWLA 58th Annual Logging Symposium. In: https://onepetro.org/SPWLAALS/proceedings/SPWLA17/5-SPWLA17/28606.

Valckenborg, R.M.E., Huinink, H.P., Sande, J.J.v.d., et al., 2002. Random-walk simulations of NMR dephasing effects due to uniform magnetic-field gradients in a pore. Phys. Rev. 65 (2), 021306. https://doi.org/10.1103/PhysRevE.65.021306.

Wang, Y., Dai, Z., Chen, L., et al., 2023. An integrated multi-scale model for CO_2 transport and storage in shale reservoirs. Appl. Energy 331, 120444. https://doi.org/10.1016/j.apenergy.2022.120444.

Xu, S., Sun, Y., Guo, W., et al., 2023. Regulating the oxidative assisted pyrolysis of Huadian oil shale by preheating temperature and oxygen flow rate. Energy 262, 125602. https://doi.org/10.1016/j.energy.2022.125602.

Yang, Y.F., Liu, Z.H., Yao, J., et al., 2018. Pore space characterization method of shale matrix formation based on superposed digital rock and pore-network model. Scientia sinica Technologica 48 (5), 488–498 (in Chinese). https://doi.org/10.1360/N092017-00076.

Zamiri, M.S., MacMillan, B., Marica, F., et al., 2021. Petrophysical and geochemical evaluation of shales using magnetic resonance T_1-T_2* relaxation correlation. Fuel 284, 119014. https://doi.org/10.1016/j.fuel.2020.119014.

Zamiri, M.S., Guo, J., Marica, F., et al., 2022. Characterization of kerogen in shale core plugs using T_2*-based magnetic resonance methods. Fuel 324, 124573. https://doi.org/10.1016/j.fuel.2022.124573.

Zamiri, M.S., Guo, J.F., Marica, F., et al., 2023. Shale characterization using T_1-T_2* magnetic resonance relaxation correlation measurement at low and high magnetic fields. Petrophysics. SPWLA J. Formation Evaluation Reserv. Descr. 64 (3), 384–401. https://doi.org/10.30632/PJV64N3-2023a5.

Zhang, K., Jia, N., Li, S., et al., 2019. Static and dynamic behavior of CO_2 enhanced oil recovery in shale reservoirs: experimental nanofluidics and theoretical models with dual-scale nanopores. Appl. Energy 255, 113752. https://doi.org/10.1016/j.apenergy.2019.113752.

Zhang, X., Li, L., Su, Y., et al., 2023. Microfluidic investigation on asphaltene interfaces attempts to carbon sequestration and leakage: Oil-CO_2 phase interaction characteristics at ultrahigh temperature and pressure. Appl. Energy 348, 121518. https://doi.org/10.1016/j.apenergy.2023.121518.

Zhou, G., Guo, Z., Sun, S., et al., 2023. A CNN-BiGRU-AM neural network for AI applications in shale oil production prediction. Appl. Energy 344, 121249. https://doi.org/10.1016/j.apenergy.2023.121249.

Zou, C.N., Zhang, G.Y., Tao, S.Z., et al., 2010. Geological features, major discoveries and unconventional petroleum geology in the global petroleum exploration. Petrol. Explor. Dev. 37 (2), 129–145. https://doi.org/10.1016/S1876-3804(10)60021-3.